

Group 13 Lewis Acid Catalyzed Synthesis of Cu₂O Nanocrystals via Hydroxide Transmetallation

Noah J. Gibson[†], Alexandria R. C. Bredar[†], Byron H. Farnum*

Department of Chemistry and Biochemistry, Auburn University, Auburn, AL 36849

*corresponding author

[†]Equal Contribution

Abstract

The colloidal synthesis of metal oxide nanocrystals (NCs) in oleyl alcohol requires the metal to catalyze an esterification reaction with oleic acid to produce oleyl oleate ester and M-OH monomers, which then condense to form M_xO_y solids. Here we show that the synthesis of Cu₂O NCs by this method is limited by the catalytic ability of copper to drive esterification and thus produce Cu⁺-OH monomers. However, inclusion of 1-15 mol% of a group 13 cation (Al³⁺, Ga³⁺, or In³⁺) results in increased yields for the consumption of copper ions toward Cu₂O formation and exhibits size/morphology control based on the nature of M³⁺. Using a continuous-injection procedure where the copper precursor (Cu²⁺-oleate) and catalyst (M³⁺-oleate) are injected into oleyl alcohol at a controlled rate, we are able to monitor the reactivity of the precursor and M³⁺ catalyst using UV-visible and FTIR absorbance spectroscopies. These time-dependent measurements clearly show that M³⁺ catalysts drive esterification to produce M³⁺-OH species, which then undergo transmetallation of hydroxide ligands to generate Cu⁺-OH monomers required for Cu₂O condensation. Ga³⁺ is found to be the “goldilocks” catalyst, producing NCs with the smallest size and a distinct cubic morphology not observed for any other group 13 metal. This is believed to be due to rapid transmetallation kinetics between Ga³⁺-OH and Cu⁺-oleate. These studies introduce a new mechanism for the synthesis of metal oxides where inherent catalysis by the parent metal (*i.e.* copper) can be circumvented with the use of a secondary catalyst to generate -OH ligands.

Introduction

The colloidal synthesis of nanocrystalline solids is a highly active area of research given that many nanocrystalline materials have unique properties for applications in optical, photochemical/photocatalytic, and electrochemical/electrocatalytic fields.^{1,2} The synthetic methods developed for these materials often involve a high level of control on the composition, morphology, and size of the nanocrystals (NCs) generated.^{2,3} The most investigated methods have been based on heat-up or hot-injection procedures which are typically done in organic solvents toward the synthesis of metal chalcogenide semiconductors.^{4,5} Each method operates under similar principles where the reaction of precursor molecules with a solvent and a surfactant leads to a nucleation event followed by NC growth, as described by the LaMer mechanism⁶, although more recently the theory of NC growth has been expanded due to the complexities of the precursors and reaction environments.⁷

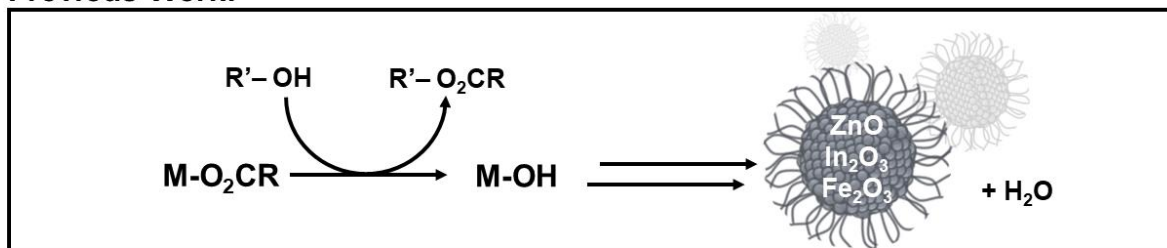
The hot-injection method relies on a fast injection of precursor molecules into the reaction solution and requires rapid reactivity of the precursor to ensure a single nucleation event. However, the scale-up of the synthesis is challenging because of its reliance on uniform mixing to achieve a single nucleation event and homogeneous cooling of the reaction to separate nucleation and growth. The heat-up synthesis method does not suffer from these setbacks because all reaction components are present upon heating of the reaction, simplifying issues with scale-up. However, secondary nucleation events are more likely to occur because of sustained monomer generation, which can overlap the growth and nucleation stages of the reaction, broadening nanocrystal size. The heat-up synthesis also requires careful tailoring of precursor reactivity, particularly with respect to formation of ternary and quaternary NCs.

More recently, a continuous-injection method has been developed for metal oxide NCs and has shown great promise for controlled generation of a wide variety of materials.⁸ While both the hot-injection and continuous-injection methods introduce precursor molecules to a pre-heated reaction solution, the continuous-injection is performed with a slower, controlled injection rate such that addition of the entire precursor volume can take multiple minutes to achieve. Instead of rapid nucleation and growth observed during fast hot-injection, the continuous-injection method allows for a layer-by-layer growth of NCs and fine control of size, morphology, and doping.⁸⁻¹²

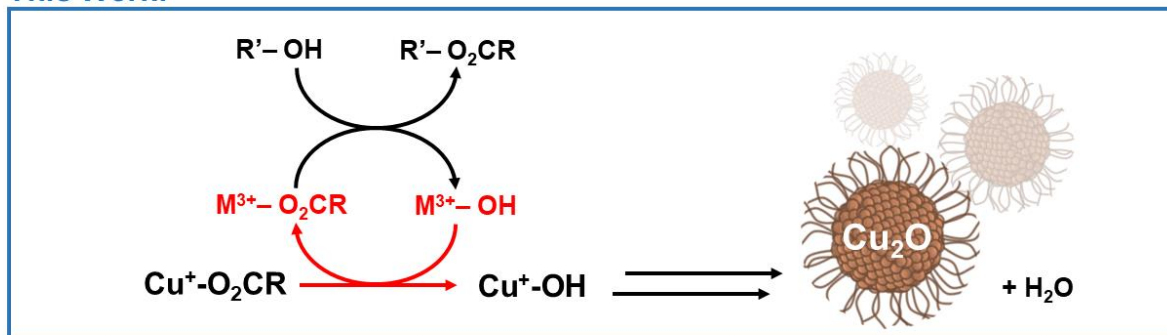
For the synthesis of metal oxides, the reaction proceeds via metal-catalyzed esterification of long-chain carboxylic acids with long-chain alcohols to produce the corresponding ester and metal

hydroxide (M-OH) monomers (**Scheme 1**, top). Most commonly, the acid and alcohol of choice are oleic acid (HO_2CR , $\text{R} = \text{R}' = \text{C}_{17}\text{H}_{33}$) and oleyl alcohol (HOR' , $\text{R}' = \text{C}_{18}\text{H}_{35}$). M-OH monomers then condense to form metal oxide NCs with water as a byproduct. The successful synthesis of nanocrystals using the continuous-injection method relies on the ability of the precursor metal to catalyze the esterification reaction to form M-OH in addition to the proclivity of M-OH monomers to undergo condensation to form a metal oxide. A wide variety of metal oxide NCs have been synthesized with this method, including In_2O_3 , CoO , Mn_3O_4 , Fe_2O_3 , and ZnO .^{8,13-15} The doping of In_2O_3 with different metals (*e.g.* $\text{Sn}:\text{In}_2\text{O}_3$) and the generation of core-shell NCs have established the versatility of this method.^{8-10,16}

Previous Work:



This Work:



Scheme 1. Reaction schemes for metal oxide NC synthesis. (top) Metal oleate ($\text{M}-\text{O}_2\text{CR}$) catalyzed esterification produces metal hydroxide ($\text{M}-\text{OH}$) monomers which undergo condensation to form metal oxide NCs. (bottom) Synthesis of Cu_2O NCs is achieved through an alternative catalytic route in which esterification by a group 13 metal cation results in transmetallation of hydroxide ligands from $\text{M}^{3+}-\text{OH}$ to produce Cu^+-OH monomers.

Despite the wide range of accessible materials, Ito *et. al.* previously found that NCs consisting of antimony, copper, and silver could not be produced using the continuous-injection method.⁸ This is seemingly due to the inability of these metals to catalyze the necessary esterification

reaction to form M-OH monomers. This indicates that more research is needed to understand the different catalytic rates of metals toward esterification and the types of NCs they generate.

Here, we report the direct synthesis of Cu₂O NCs smaller than 100 nm using the continuous-injection method. The key to our approach is the presence of catalytic amounts (1-15 mol%) of Al³⁺, Ga³⁺, or In³⁺ cations. The introduction of cations and inorganic complexes to tune reactivity is not unusual in the metal chalcogenide literature¹⁷⁻¹⁹, but typically the addition of these species changes resultant nanoparticle morphology and not necessarily precursor reactivity. We find that addition of these metals to our system allows for efficient esterification catalysis to produce M³⁺-OH species. The hydroxide ligand is then transmetallated from M³⁺-OH to form Cu⁺-OH monomers (**Scheme 1**, bottom), thus bypassing the copper-catalyzed esterification route which is found to be much slower than M³⁺-catalysis. These Cu⁺-OH monomers then quickly condense to form Cu₂O NCs.

Spectroscopic data (UV-visible and FTIR) collected during and following the injection process provide detailed information about the formation of oleyl oleate ester and the consumption of the copper oleate (Cu²⁺-O₂CR) precursor over time. These studies point to a new mechanism for metal oxide synthesis in which the generation of a metal oxide NC is not limited by the inherent reactivity of the parent metal (*i.e.* Cu) toward esterification to produce M-OH monomers. Instead, the monomers can be generated by transmetallation from a secondary M³⁺-OH species produced from esterification catalyzed by a group 13 metal cation. These studies also highlight the competitive and independent reactivity of two metal cations in the same solution and are therefore important for the synthesis of more complex ternary metal oxide NCs.

Experimental

Materials Oleic acid (technical grade, 90%), and oleyl alcohol (technical grade, 80-85%) were purchased from Alfa Aesar and used as received. Copper (II) acetate (Cu(OAc)₂, 98%), indium (III) acetylacetonate (In(acac)₃, 99.99%), aluminum (III) acetylacetonate (Al(acac)₃, 99.99%), gallium (III) acetylacetonate (Ga(acac)₃, 99.99%) were purchased from Sigma-Aldrich and used as received. To monitor the nitrogen (99.999%, Airgas) flow rate, a Cole-Parmer flow meter (model PMR1-010270) was utilized. A syringe pump from New Era Pump Systems, Inc (Model NE-4000) was used to control injection rate.

General Synthesis of Copper(I) Oxide Nanocrystals To synthesize Cu₂O NCs, Cu(OAc)₂ (2.45 mmol) and 0, 1, 5, 10, or 15 mol% of Al(acac)₃, Ga(acac)₃, or In(acac)₃ was placed in a 25 mL 3-neck round bottom flask with 5 mL of oleic acid to result in a 0.49 M [Cu(OAc)₂] mixture. This flask was then capped with three rubber septa and the mixture was heated to 150 °C under nitrogen flow with constant stirring for thirty minutes to produce copper oleate precursor (Cu²⁺-O₂CR) and the corresponding M³⁺-O₂CR catalyst. This step also facilitates the removal of any acetic acid or acetylacetone through evaporation. In a separate 100 mL 3-neck round bottom flask, 25 mL of oleyl alcohol was heated to 200 °C while nitrogen was flowed over the solvent. The precursor solution was allowed to cool to 90 °C before 4 mL of the solution (equivalent to 1.96 mmol of Cu²⁺-O₂CR) was then drawn into a 10 mL syringe and injected into the oleyl alcohol at a rate of 0.35 mL min⁻¹ using a syringe pump. The reaction flask was constantly stirred during and after injection and the solution was held at 200 °C for 5 minutes after the injection was completed. The flask was then removed from heat and slowly cooled to room temperature.

The reaction mixture was centrifuged at 7500 rpm for 10 minutes to separate the solid product and supernatant. The supernatant was collected for further spectroscopic analysis. The solid was washed using 15 mL of hexanes and sonicated using an ultra-sonication horn (Branson 150) for resuspension. An equal volume of acetone was added to precipitate particles in solution. This was followed by centrifugation at 7500 rpm for 5 minutes. The washing and centrifugation steps were repeated 3 times. The resulting solid was dried from acetone in a vacuum oven for characterization. Solid isolation and washing were performed under ambient conditions.

Characterization of Copper(I) Oxide Nanocrystals and Post-Reaction Solutions Solid state materials resulting from the synthesis were characterized using multiple techniques. Powder X-ray diffraction (PXRD, Rigaku SmartLab, Cu K α) was used to assess phase and crystallinity of the synthesized materials. Diffractograms were collected and compared to a Cu₂O standard (PDF #01-078-2076). Scanning electron microscopy (SEM, Hitachi S-4700 Field Emission Microscopy) and transmission electron microscopy (TEM, Thermofisher Talos F200X, lacey carbon on gold TEM grid) were used to assess particle size and morphology. Energy Dispersive Spectroscopy (EDS, Super-X EDS attached to TEM) was used to determine elemental composition. SEM, TEM, and EDS were performed at the Chapel Hill Analytical and Nanofabrication Laboratory.

The post-reaction solution (*i.e.* supernatant from initial centrifugation) was characterized to understand the extent of reactivity with each M³⁺ catalyst using attenuated total reflectance Fourier

transform infrared (ATR-FTIR) spectroscopy (Nicolet iS-50 with built-in ATR) and UV-visible absorbance spectroscopy (Agilent Cary 5000, thin path length (0.2 cm) glass cuvette). For ATR-FTIR measurements, a liquid drop of post-reaction solution was placed directly on diamond ATR crystal.

Time Dependent Copper(I) Oxide Synthesis For kinetic analysis of the Cu₂O synthesis, the reaction was performed as described above, but with small aliquots (100-200 μ L) removed from the reaction approximately every thirty seconds during the injection period, and every minute after the conclusion of the injection period. These aliquots were analyzed via ATR-FTIR by directly adding liquid drops of each aliquot on the ATR crystal. UV-visible absorbance measurements for the aliquots were collected by diluting 100 μ L of aliquot with 900 μ L of oleyl alcohol.

Results and Discussion

Cu₂O Synthesis Cu₂O nanocrystals were synthesized by a continuous-injection procedure. Cu(OAc)₂ and the appropriate M(acac)₃ salt were first combined in oleic acid (HO₂CR, R= C₁₇H₃₃) and heated at 150 °C for a minimum of 30 minutes to generate Cu²⁺-O₂CR and M³⁺-O₂CR species. The amount of Cu²⁺-O₂CR, also referred to as the precursor, used for each experiment was constant at 1.96 mmol. The concentration of M³⁺-O₂CR catalysts, also referred to as M³⁺, were varied based on mol% of the precursor. 4 mL of the prepared precursor/catalyst solution was then injected at a controlled rate of 0.35 mL/min into oleyl alcohol at 200 °C. After completion of the injection, the temperature was held at 200 °C for 5 minutes to allow for the reaction of any remaining precursor before the flask was removed from the hot plate and allowed to slowly cool to room temperature. Solid products were isolated from the final solution following multiple washing/extraction steps.

Figure 1a shows PXRD data collected for solid products resulting from 10 mol% Al³⁺, Ga³⁺, and In³⁺, compared with 0 mol% catalyst. PXRD data for all catalyst conditions are shown in **Figure S1**. For Ga³⁺ and In³⁺ reactions, Cu₂O is the exclusive product with no evidence of side products such as CuO or M₂O₃. For some reaction conditions, Cu⁰ was produced as a minor product. Conditions which favored the production of Cu⁰ included elevated temperatures (>215 °C, **Figure S2**), slow injection rates, and extended times following injection at which the reaction remained at high temperature. We also note that Cu⁰ was produced for >5 mol% Al³⁺ (**Figure S1**). The Cu₂O observed when Cu⁰ metal was present was green in color, as opposed to the

yellow/orange solid produced when no Cu^0 was present. The green colored solid has been attributed to a Cu^0 core with a Cu_2O shell.²⁰

The fact that Cu_2O is observed instead of CuO indicates that oleyl alcohol acts as a sufficient reductant for the conversion from Cu^{2+} to Cu^+ during the reaction. Evidence for alcohol reduction of copper has previously been reported in the literature.²¹ Given that CuO is not produced in any detectable quantity, we also believe that copper reduction occurs prior to nanocrystal formation such that Cu_2O is formed directly from Cu^+ -OH monomers. In fact, if the reaction temperature was held below 200 °C, no solid formation occurred and the reaction solution stayed green in color, indicating that Cu^{2+} was never reduced. Attempts to use a Cu^+ precursor (*i.e.* $\text{Cu}(\text{OAc})$) as a starting material were unsuccessful, as the exchange of acetate and oleate ligands oxidized Cu^+ to Cu^{2+} with the resulting precursor solution having the same absorbance spectrum and color as Cu^{2+} - O_2CR (**Figure S3**).

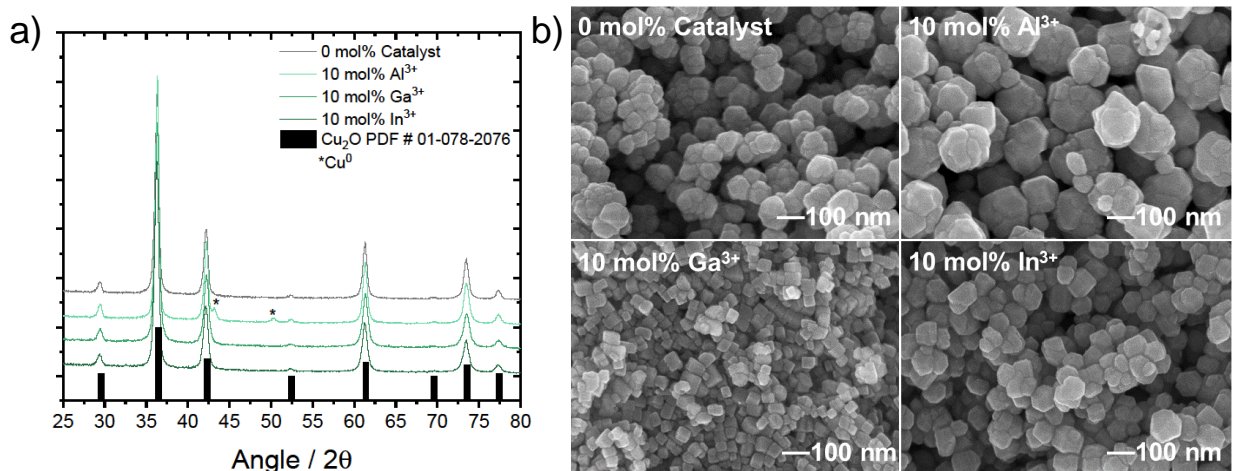


Figure 1. a) PXRD data collected for Cu_2O NCs synthesized by continuous-injection of Cu^{2+} - O_2CR as a function of 0 mol% and 10 mol% Al^{3+} , Ga^{3+} , or In^{3+} catalyst loading at 200 °C under N_2 . A standard diffraction pattern for Cu_2O (PDF# 01-078-2076) is shown for comparison. b) SEM images of Cu_2O NCs synthesized in the absence (0 mol%) and presence of 10 mol% M^{3+} catalysts.

In terms of M^{3+} oxide side products, we note that the synthesis of In_2O_3 has been heavily explored with the continuous-injection method.^{8-11,16,22} However, the low concentrations of In^{3+} used in these studies does not yield In_2O_3 product. For example, control experiments using only M^{3+} - O_2CR up to 0.30 mmol (equivalent to 15 mol% catalyst loading) showed no solid formation for any of

the group 13 metal cations. However, injection of $\text{In}^{3+}\text{-O}_2\text{CR}$ and $\text{Ga}^{3+}\text{-O}_2\text{CR}$ at 2 mmol (equivalent to 100 mol% catalysts loading) did yield nanocrystalline In_2O_3 and $\gamma\text{-Ga}_2\text{O}_3$ (**Figure S4**). Similar experiments for Al^{3+} at 100 mol% were unsuccessful, as the precursor solidified in the syringe at high concentrations, making it impossible to inject.

SEM images of NCs produced with 0 mol% catalyst and 10 mol% Al^{3+} , Ga^{3+} , or In^{3+} are shown in **Figure 1b**. SEM images for 1, 5, and 15 mol% catalysts are shown in **Figure S5**. NC sizes for different mol% are given in **Table 1** and **Figure S6**. With no catalysts present, Cu_2O NCs were found to be roughly spherical with minor faceting and an average size of 129 ± 27 nm. NC agglomeration was also observed and believed to be due to weak coordination of oleate ligands to the Cu_2O surface. This observation was consistent across all reaction conditions. As a function of M^{3+} catalyst, clear differences in the size and morphology of Cu_2O NCs were observed. In general, the size of NCs was found to increase in the order $\text{Ga}^{3+} < \text{In}^{3+} < \text{Al}^{3+}$. Cu_2O produced from Ga^{3+} also exhibited a distinct cubic morphology while NCs resulting from In^{3+} and Al^{3+} were more spherical in shape, similar to those produced in the absence of M^{3+} cations. The change in the morphology with the addition of Ga^{3+} specifically points to a unique change in the kinetics of Cu_2O formation discussed further below. For all M^{3+} cations, no significant trends were observed between NC size and mol% catalyst. TEM images for all reaction conditions are shown in **Figure S7-S15**. EDS performed in combination with TEM revealed no evidence for In, Ga, or Al atoms within Cu_2O NCs. This result indicates that M^{3+} cations are not doped into Cu_2O nor do they form seed particles from which Cu_2O grows.

Table 1. Cu_2O NC sizes (nm)

No Catalyst		0 mol%		
$\text{Cu}^{2+}\text{-O}_2\text{CR}$		129 ± 27		
With Catalyst	1 mol%	5 mol%	10 mol%	15 mol%
Al^{3+}	169 ± 30	96 ± 15	191 ± 22	168 ± 43
Ga^{3+}	62 ± 11	64 ± 13	58 ± 13	72 ± 16
In^{3+}	111 ± 19	117 ± 17	90 ± 17	85 ± 14

Despite the noted changes in Cu_2O NC size and morphology with M^{3+} cations, it is not apparent from PXRD or microscopy data that these metals are acting catalytically for Cu_2O formation.

However, UV-visible absorbance and FTIR spectroscopy provide compelling evidence for this assignment and offer new insights into possible mechanisms for metal oxide formation. **Figure 2** shows UV-visible absorbance spectra obtained from post-reaction solutions for each catalyst. These spectra show a peak at 695 nm consistent with the Cu^{2+} - O_2CR precursor. The 0 mol% condition resulted in post-reaction solutions which are deep green in color due to the strong peak at 695 nm. As catalysts were introduced, the intensity of the green color diminished as the peak decreased, finally resulting in a yellow amber color as the peak completely disappeared.

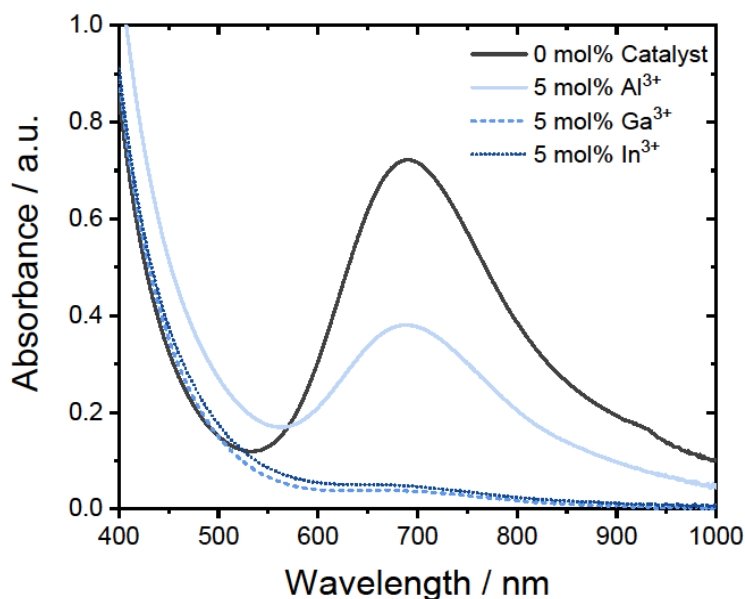


Figure 2. UV-visible absorbance spectra of post-reaction solutions obtained from continuous-injection of Cu^{2+} - O_2CR with 0 mol% and 5 mol% Al^{3+} , Ga^{3+} , or In^{3+} at 200 °C under N_2 . The peak at 695 nm is indicative of unreacted Cu^{2+} - O_2CR precursor remaining in solution. Absorbance was corrected for oleyl alcohol.

The magnitude of the 695 nm peak in the post-reaction solution can be used to measure reaction efficiency with the equation $\eta_{\text{rxn}} = 1 - [\text{Cu}^{2+}]_{\text{unreacted}}/[\text{Cu}^{2+}]_{\text{total}}$. The concentration of unreacted precursor was calculated for these solutions based on the extinction coefficient of the 695 nm peak (**Figure S16**). In the case of 0 mol% catalyst, $[\text{Cu}^{2+}]_{\text{unreacted}} = 17$ mM, resulting in $\eta_{\text{rxn}} = 76\%$ based on a $[\text{Cu}^{2+}]_{\text{total}} = 68$ mM present in the oleyl alcohol/oleic acid solution after injection. Upon addition of 5 mol% Al^{3+} , Ga^{3+} , or In^{3+} , $[\text{Cu}^{2+}]_{\text{unreacted}}$ decreased to 8.2, 4.4, and 5.9 mM, corresponding to $\eta_{\text{rxn}} = 86, 99,$ and 98% , respectively. In the case of Al^{3+} , the 695 nm peak remained present for all mol% catalyst conditions, indicating incomplete reactivity. $[\text{Cu}^{2+}]_{\text{unreacted}}$

was never less than 7 mM with the addition of up to 15 mol% Al^{3+} , resulting in a maximum $\eta_{\text{rxn}} = 90\%$. (**Figure S17**) With Ga^{3+} or In^{3+} , η_{rxn} achieved $>98\%$ for ≥ 5 mol% catalyst loading.

Figure 3 shows a summary of FTIR spectra collected for post-reaction solutions as a function of mol% catalyst. Previous literature reports have used FTIR to evaluate the esterification reaction using peaks consistent with free oleic acid (1710 cm^{-1}), oleyl oleate ester (1738 cm^{-1}) and oleyl alcohol (3300 cm^{-1}).⁸ **Figure 3** clearly shows the presence of these species in addition to $\text{Cu}^{2+}\text{-O}_2\text{CR}$, identified by the C=O stretch of the bound oleic acid at 1620 cm^{-1} , and an unknown solvent peak at 1660 cm^{-1} likely due to impurity (notably, this peak was constant as a function of reaction conditions, indicating no reactivity in the esterification cycle). Based on FTIR data, all M^{3+} catalysts showed greater reactivity than $\text{Cu}^{2+}\text{-O}_2\text{CR}$ for the conversion of oleic acid to oleyl oleate ester. Consistent with data from UV-visible absorbance, Al^{3+} showed little variation in ester formation as a function of mol% and incomplete consumption of $\text{Cu}^{2+}\text{-O}_2\text{CR}$ (**Figure S18**). Ga^{3+} and In^{3+} both showed significant consumption of the oleic acid peak and the $\text{Cu}^{2+}\text{-O}_2\text{CR}$ precursor in addition to formation of the ester peak.

Notably, these data were collected using an ATR-FTIR instrument, and while this is normally not a quantitative method, the low vapor pressure and high viscosity of the oleyl alcohol solvent allowed for a consistent sample volume to be obtained on top of the ATR crystal. Although we do not know the exact path length for the evanescent wave, Beer-Lambert plots of oleic acid (1710 cm^{-1}) and $\text{Cu}^{2+}\text{-O}_2\text{CR}$ (1620 cm^{-1}) (**Figure S19-S20**) were found to be linear over the absorbance range shown in **Figure 3** and allowed for apparent extinction coefficients of $\epsilon_{\text{app}} = 0.16\text{ M}^{-1}$ and 0.56 M^{-1} to be estimated for each peak, respectively. In a separate experiment, the apparent extinction coefficient for oleyl oleate ester at 1738 cm^{-1} was determined to be $\epsilon_{\text{app}} = 0.20\text{ M}^{-1}$ by converting 100% of oleic acid molecules to oleyl oleate ester by heating to $230\text{ }^\circ\text{C}$ in the presence of excess oleyl alcohol and no metal catalysts (**Figure S21**). These values allow for a reliable estimation of the concentrations of reactants and products for the esterification reaction which are discussed further below with respect to time-dependent FTIR experiments.

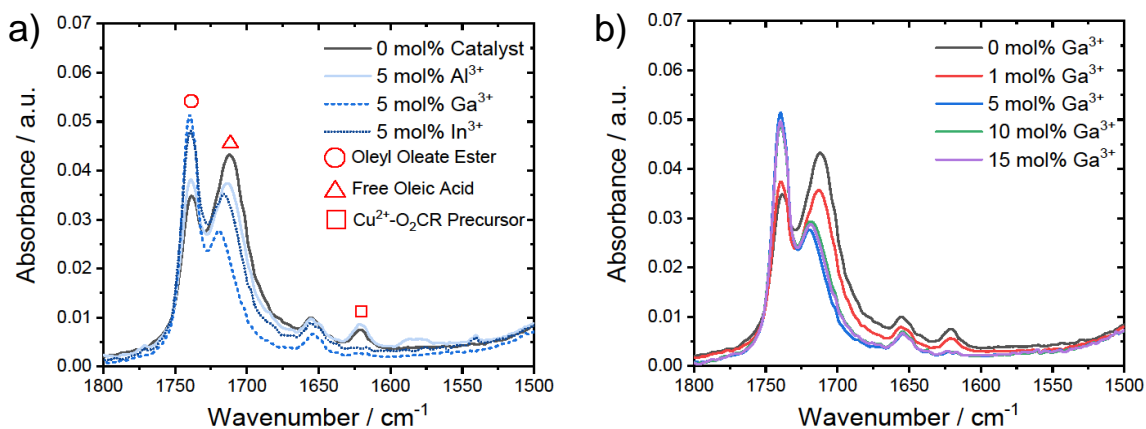


Figure 3. a) FTIR absorbance spectra in the C=O region of post-reaction solutions obtained from continuous-injection of $\text{Cu}^{2+}\text{-O}_2\text{CR}$ with 0 mol% and 5 mol% Al^{3+} , Ga^{3+} , or In^{3+} at 200 °C under N_2 . b) Similar data comparing 0-15 mol% Ga^{3+} catalyst loading conditions.

Time-Dependent Experiments The decrease in unreacted Cu^{2+} ions observed by UV-visible absorbance spectroscopy coupled with the enhanced production of oleyl oleate ester observed by FTIR points to a catalytic mechanism for the formation of Cu_2O in the presence of group 13 metals. To gain more insight, we performed time dependent experiments where 100-200 μL aliquots were removed from the reaction solution over a 17-minute time window. These aliquots were then analyzed by FTIR and UV-visible absorbance spectroscopy to observe the consumption of oleic acid and $\text{Cu}^{2+}\text{-O}_2\text{CR}$ precursor while watching the evolution of oleyl oleate ester over time. **Figure 5** shows FTIR data for the reaction performed with 5 mol% Ga^{3+} . Similar data are shown in **Figure S22** for 0 mol% catalyst, 1 mol% Ga^{3+} , 10 mol% Ga^{3+} , 5 mol% Al^{3+} , and 5 mol% In^{3+} reactions. Note that data are plotted as ΔAbs with respect to the initial spectrum at 0 min, which represents an aliquot removed from the oleyl alcohol solution just before injection began. Over the course of 17 min, these data collectively show the consumption of oleyl alcohol (3300 cm^{-1}) concomitant with the growth of oleyl oleate ester (1738 cm^{-1}). Peaks associated with free oleic acid (1710 cm^{-1}) and $\text{Cu}^{2+}\text{-O}_2\text{CR}$ precursor (1620 cm^{-1}) were found to increase initially as these species were injected into solution, but eventually decayed over time as the esterification reaction and consumption of $\text{Cu}^{2+}\text{-O}_2\text{CR}$ progressed.

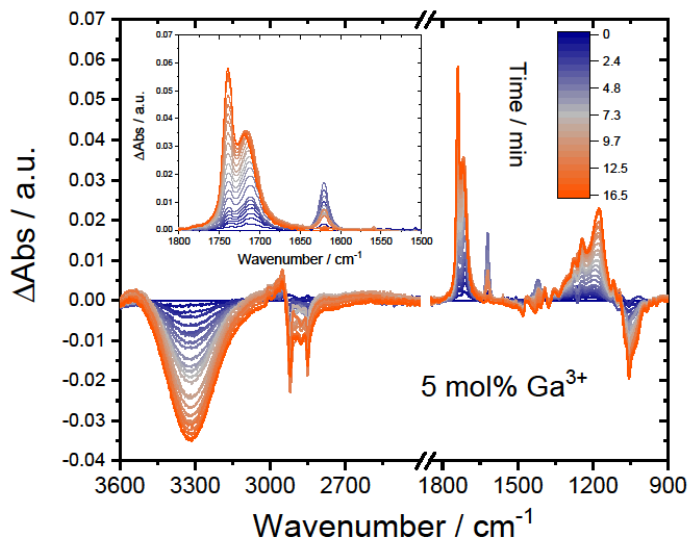


Figure 5. FTIR Δ Abs spectra collected for aliquots of reaction solution removed as a function of time during continuous-injection of Cu^{2+} - O_2CR with 5 mol% Ga^{3+} at 200 °C under N_2 .

By analyzing changes in these peaks with respect to time we can see several trends that occur with each catalyst and mol%. **Figure 6a-b** show the Cu^{2+} - O_2CR precursor peak intensity at 1620 cm^{-1} as a function of time for different mol% Ga^{3+} and comparing 5 mol% for each group 13 metal. The rate for the initial buildup of precursor is consistent across all experiments due to the controlled injection rate of 0.35 mL/min, which is completed at the 11.5 min mark based on an injection volume of 4 mL. A 0 mol% catalyst injection performed at 25 °C is shown for comparison to highlight the rate of precursor growth and maximum concentration of precursor obtained in the absence of esterification or NC formation. Note that the measured maximum concentration of 75 mM represents a 10% increase from the expected concentration of 68 mM. This was a result of decreased volume from the ~25 aliquots removed from solution during the experiment. Across all reaction conditions, buildup of the precursor is shown to reach a critical limit before being consumed. The time point where consumption begins is consistent with where product formation is observed visually in the experiment as the solution changes from green to yellow. This was also confirmed by UV-visible absorbance spectroscopy by the peak observed at 490 nm, consistent with Cu_2O (**Figure S23**).²³ This time point was found to decrease from 9.2 min for 0 mol% Ga^{3+} to 5.5, 4.6, and 4.3 min for 1, 5, and 10 mol% Ga^{3+} , respectively. Among the group 13 metals, this time point was found to decrease in the order Al^{3+} (8.9 min) < In^{3+} (4.9 min) < Ga^{3+} (4.6 min) for the 5 mol% condition.

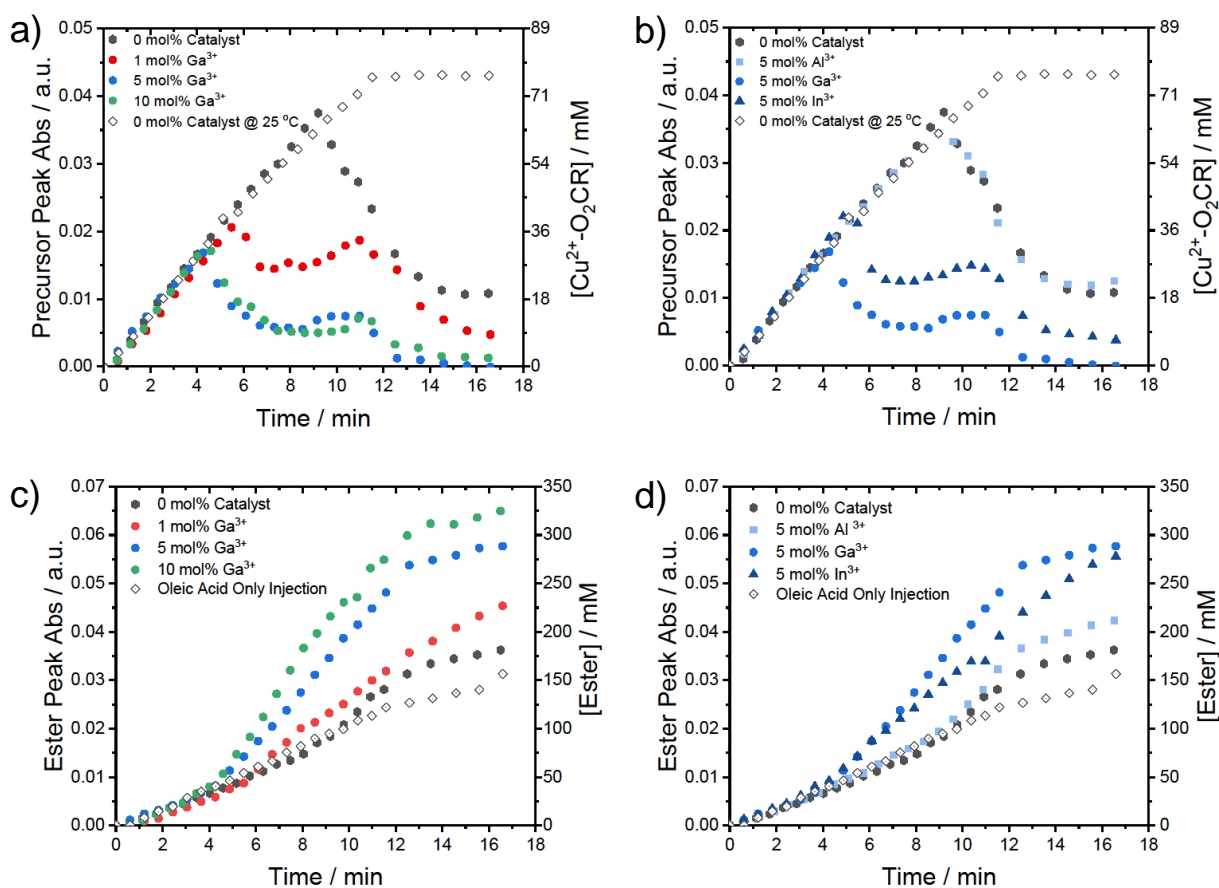


Figure 6. a-b) Precursor peak absorbance at 1620 cm^{-1} obtained from time-dependent FTIR measurements comparing 0-10 mol% Ga^{3+} and different group 13 cations at 5 mol%. c-d) Ester peak absorbance at 1738 cm^{-1} obtained from time-dependent FTIR measurements comparing 0-10 mol% Ga^{3+} and different group 13 cations at 5 mol%. Precursor and ester concentrations were calculated from apparent extinction coefficients obtained from **Figures S19-S21**.

In the cases of Ga^{3+} and In^{3+} , the precursor peak intensity reached steady-state around 7 min before rising again around 8-9 min and eventually decaying to lower values after 11 min. We believe this observation reflects the balance in rates between addition of the precursor/catalyst via injection and consumption via NC formation. Following the first decrease in precursor concentration, the rate of NC formation likely decreased with time and was equal to the injection rate around the 7 min mark. The rise in precursor around 8-9 min was therefore due to the rate of precursor consumption dropping below the rate of the injection, thus a net addition of precursor

was observed. When the injection was completed around 11 min, the precursor concentration decreased again because the rate of consumption was uncontested.

Figure 6c-d show time dependent FTIR data for the oleyl oleate ester peak intensity at 1738 cm⁻¹. Clear changes in the rate of ester formation are observed as a function of mol% Ga³⁺ and the nature of the group 13 metal. In all cases, the linear increase in Abs₁₇₃₈ between 0-4 min was due to background esterification as shown for the injection of oleic acid into oleyl alcohol at 200 °C in the absence of any metal (**Equation 1**, R = C₁₇H₃₃, R' = C₁₈H₃₅). The apparent rate for this background process was estimated to be 11 mM min⁻¹ based on the linear slope from 0-11 min. The apparent zero-order nature of ester growth is likely due to the excess concentration of oleyl alcohol and the constant replenishment of oleic acid due to the slow injection rate. The total concentration of ester produced by **Equation 1** over the 17 min time window was found to be [Ester]_{final} = 94 mM, equivalent to 24% conversion of injected oleic acid.

- 1) H-O₂CR + R'-OH → R'-O₂CR + H-OH
- 2) M-O₂CR + R'-OH → R'-O₂CR + M-OH

As the precursor/catalyst solution was injected, metal catalyzed esterification became an additional pathway for ester production (**Equation 2**), as indicated by the changes in rate observed at 10, 6, 4, and 4 min for 0, 1, 5, and 10 mol% Ga³⁺, respectively. These time points were also found to coincide with the sharp decrease in the precursor peak, indicating that consumption of the precursor was triggered by metal catalysis. Furthermore, control experiments performed with 5 mol% Ga³⁺ in the absence of Cu²⁺-O₂CR exhibited the same rate for ester formation and total ester produced as when Cu²⁺-O₂CR was present (**Figure S24**), indicating that esterification is dominated by Ga³⁺ catalysis. The rates for metal catalyzed esterification were also found to be zero-order and were estimated to be 24, 20, 28, and 38 mM min⁻¹ for 0, 1, 5, and 10 mol% Ga³⁺ based on the linear portion of ester growth immediately following the onset of metal catalysis. The [Ester]_{final} produced also increased with mol% Ga³⁺ from 125 mM for 0 mol% to 183, 260, and 307 mM for 1, 5, and 10 mol%, respectively. These data indicate a clear dependence on [Ga³⁺] for the esterification reaction.

A comparison of group 13 metals at 5 mol% loading revealed that Al³⁺ catalyzed the esterification reaction only slightly better than Cu²⁺-O₂CR on its own, with a rate of 27 mM min⁻¹

and $[\text{Ester}]_{\text{final}} = 163 \text{ mM}$ (**Table 2**). The $[\text{Ester}]_{\text{final}}$ produced for Ga^{3+} (260 mM) and In^{3+} (247 mM) were much larger, but with comparable rates of 28 and 21 mM min^{-1} , respectively.

Turnover numbers (TON) for each catalyst were estimated by the equation $\text{TON} = [\text{Ester}]_{\text{cat}}/[\text{Cat}]$, where $[\text{Ester}]_{\text{cat}} (= [\text{Ester}]_{\text{final}} - [\text{Ester}]_{\text{final(oleic acid)}}$) is the concentration of ester produced by each catalyst and $[\text{Cat}]$ is the total concentration of each metal ion in the reaction solution following injection. For example, at the 5 mol% condition, $[\text{Cu}^{2+}] = 75 \text{ mM}$ and $[\text{M}^{3+}] = 3.8 \text{ mM}$. Resulting TON's showed that Ga^{3+} was the best group 13 catalyst with 44 ester molecules produced for every Ga^{3+} cation while Cu^{2+} achieved only 0.4 turnovers. Furthermore, TON was found to decrease with higher mol% for the Ga^{3+} series, showing that while the ester formation rate increased with more Ga^{3+} , not all cations were catalytically active. This will be discussed in detail further below.

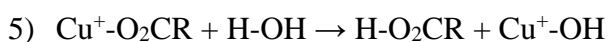
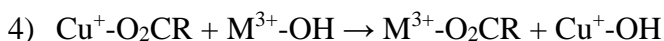
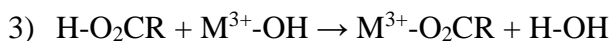
Table 2. Comparison of M^{3+} Esterification Catalysis

Reaction Condition	$\eta_{\text{rxn}}^{\text{a}}$ (%)	Ester Rate ^b (mM min^{-1})	$[\text{Ester}]_{\text{final}}^{\text{c}}$ (mM)	$[\text{Ester}]_{\text{cat}}^{\text{d}}$ (mM)	TON ^e
Oleic acid only	-	11	94	-	-
Cu^{2+} - O_2CR	76	24	125	31	0.4
1 mol% Ga^{3+}	94	20	183	89	119
5 mol% Ga^{3+}	99	28	260	166	44
10 mol% Ga^{3+}	99	38	307	213	28
5 mol% Al^{3+}	86	27	163	69	18
5 mol% In^{3+}	98	21	247	153	41

^a $\eta_{\text{rxn}} = 1 - [\text{Cu}^{2+}]_{\text{unreacted}}/[\text{Cu}^{2+}]_{\text{total}}$; ^bEstimated by the linear slope for growth of 1738 cm^{-1} FTIR peak; ^c $[\text{Ester}]_{\text{final}} = (\text{Abs}_{\text{final}}(1738 \text{ cm}^{-1}) - \epsilon_{\text{app,acid}}[\text{Acid}]_{\text{total}})/(\epsilon_{\text{app,ester}} - \epsilon_{\text{app,acid}})$ where $\epsilon_{\text{app,acid}} = 0.04 \text{ M}^{-1}$, $\epsilon_{\text{app,ester}} = 0.20 \text{ M}^{-1}$, and $[\text{Acid}]_{\text{total}} = 393 \text{ mM}$; ^d $[\text{Ester}]_{\text{cat}} = [\text{Ester}]_{\text{final}} - [\text{Ester}]_{\text{final(oleic acid)}}$; ^e $\text{TON} = [\text{Ester}]_{\text{cat}}/[\text{Cat}]$.

Catalytic Mechanism Based on the established mechanism of M-OH condensation to yield metal oxide NCs, we can reason that every copper ion present within Cu_2O must have existed as a Cu^+ -OH monomer. The generation of these monomers could arise through copper catalyzed esterification like that shown in **Equation 2** or, as we propose here, transmetallation with M^{3+} -OH species. Unfortunately, we were unable to identify a unique FTIR absorbance resulting from the M^{3+} -OH bond, therefore we use the ester peak as an indirect measure of M^{3+} -OH formation. The

large $[\text{Ester}]_{\text{cat}}$ observed for Ga^{3+} and In^{3+} indicate that $\text{Ga}^{3+}\text{-OH}$ and $\text{In}^{3+}\text{-OH}$ are produced in high quantities. Based on **Equation 2**, the total moles of $\text{M}^{3+}\text{-OH}$ produced over the lifetime of the reaction should be equal to the total moles of ester produced by the catalyst. Many of these $\text{M}^{3+}\text{-OH}$ species are converted back to $\text{M}^{3+}\text{-O}_2\text{CR}$ by reacting with oleic acid (**Equation 3**) whereby the catalyst is regenerated and may proceed through another cycle. However, in the presence of $\text{Cu}^+\text{-O}_2\text{CR}$, the transmetallation reaction shown in **Equation 4** could equally regenerate the $\text{M}^{3+}\text{-O}_2\text{CR}$ catalyst while also producing $\text{Cu}^+\text{-OH}$. Here, we indicate $\text{Cu}^+\text{-O}_2\text{CR}$ because the reaction does not proceed unless reduction of Cu^{2+} to Cu^+ occurs. Therefore, we believe that the $\text{Cu}^{2+}\text{-O}_2\text{CR}$ precursor is first reduced to $\text{Cu}^+\text{-O}_2\text{CR}$ prior to transmetallation of the -OH ligand.

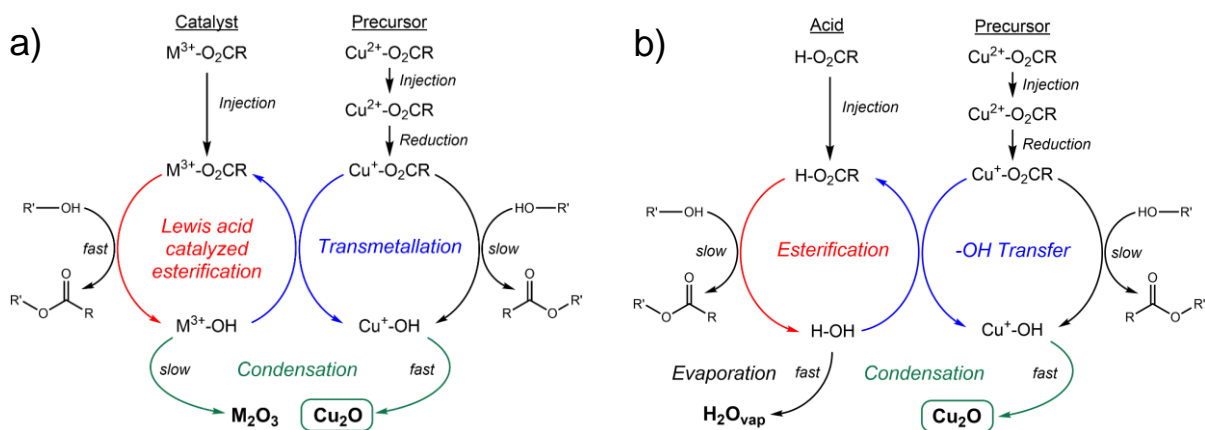


It is important to note that **Equations 3-4** are the same reaction with the only difference being the nature of the cation bound to the $\text{-O}_2\text{CR}$ ligand, H^+ vs Cu^+ . This comparison highlights the competition that exists between protons and metal cations for -OH ligands during the catalytic cycle. Control experiments which showed 5 mol% Ga^{3+} produced the same amount of ester with or without copper ions present suggest that their inclusion supplants $\text{H-O}_2\text{CR}$ as a reactant with $\text{Ga}^{3+}\text{-OH}$.

While $\text{M}^{3+}\text{-OH}$ species are suitable donors for -OH ligands, H_2O (H-OH) produced through background esterification or $\text{Cu}^+\text{-OH}$ condensation could also deliver -OH ligands and bypass the copper catalyzed esterification route (**Equation 5**). In fact, it is known that if H_2O is not efficiently removed from solution during the synthesis of In_2O_3 , then uncontrolled NC growth is observed through ligand exchange of $\text{In}^{3+}\text{-O}_2\text{CR}$ and H_2O to generate $\text{In}^{3+}\text{-OH}$ species.⁸ From **Table 2**, it is apparent that a significant amount of $\text{Cu}^+\text{-OH}$ must be generated by ligand exchange between $\text{Cu}^+\text{-O}_2\text{CR}$ and H_2O . This is evident by the fact that $\text{TON} = 0.4$ but $\eta_{\text{rxn}} = 76\%$ for the 0 mol% condition. This means that, on average, only 40% of the copper ions go through one esterification cycle to produce $\text{Cu}^+\text{-OH}$, yet 76% of copper ions are consumed to produce Cu_2O . Notably, the reaction is designed to sweep H_2O from the reaction flask due the elevated temperature (200 °C) and continuous flow of N_2 over the solution surface. Based on **Equation 5**, it could even be possible

that the copper precursor does not catalyze esterification at all, and instead, the late onset for precursor consumption could be related to a slow buildup of H₂O in solution until a critical concentration is reached.

Scheme 2 provides two catalytic cycles to summarize our proposed reactions, with and without M³⁺ catalysts. In the presence of these catalysts, M³⁺-O₂CR is able to catalyze the formation of oleyl oleate ester (R'-O₂CR) in the presence of oleyl alcohol (R'-OH) to produce M³⁺-OH species. Likewise, Cu⁺-O₂CR is able to catalyze the esterification reaction to produce Cu⁺-OH. Given that copper catalysis is observed to be less efficient than M³⁺ catalysis, we believe that most, if not all, Cu⁺-OH species are generated through transmetalation of -OH from M³⁺-OH to Cu⁺-O₂CR, defined by the central path. Once Cu⁺-OH species are formed, rapid condensation occurs to produce Cu₂O NCs. Importantly, the condensation of M³⁺-OH species is in direct competition with transmetalation and therefore the low concentration of M³⁺ catalysts is critical in preventing condensation and achieving the -OH transfer step. In the absence of M³⁺ catalysts, a mirrored reaction cycle can be shown in which oleic acid (H-O₂CR) replaces the M³⁺-O₂CR species and undergoes esterification to yield oleyl oleate ester and water (H-OH) as products. Similar to the M³⁺ cycle, water may transfer the -OH ligand to Cu⁺-O₂CR to generate Cu⁺-OH and trigger Cu₂O formation. However, unlike the M³⁺ cycle, the -OH transfer reaction is in competition with the removal of water from the solution by vaporization.



Scheme 2. a) Proposed catalytic cycle for M³⁺ catalyzed esterification to ultimately produce Cu₂O NCs through a -OH transmetalation step. b) Proposed catalytic cycle for the synthesis of Cu₂O NCs in the absence of M³⁺ catalysts.

Insights into Group 13 Catalysts Lewis acid catalyzed esterification is a well-studied reaction in the field of organic synthesis.^{24–26} The established mechanism involves activation of the organic acid by coordination of the carbonyl group to the Lewis acidic cation, thus making the carbonyl carbon more susceptible to nucleophilic attack by an alcohol.²⁷ Therefore, the coordination environment around the metal as well as its Lewis acidity play key roles in determining reactivity. Here, we have exchanged acetylacetonate ligands for oleate ligands with each group 13 metal to generate active catalysts. This was performed at elevated temperatures under inert gas; however, it is difficult to know the extent to which the ligand exchange reaction has been performed. This is especially important in the case of Al³⁺. Among the group 13 metals, Al³⁺ is the strongest Lewis acid and would be expected to be the best catalysts for esterification.²⁸ However, here we observe it as the worst catalyst, barely better than the copper precursor. We believe this is due to incomplete exchange of the acetylacetonate ligands during preparation of the catalyst, which would result in catalytically inactive Al³⁺ cations. Indeed, Al³⁺ is the hardest acid and most oxophilic among the group and would therefore be expected to strongly resist ligand exchange from the chelated acetylacetonate environment.

Further evidence that incomplete preparation of the Al³⁺ precursor could be responsible for its lack of catalysis can be found by comparing the esterification rates for each catalyst with the reaction time in which metal catalysis begins. For all metals, including copper, the esterification rate was found to be within the range of 20–30 mM min⁻¹. However, Al³⁺ catalysis did not begin until 8.9 min for the 5 mol% condition compared to 4.6 min for Ga³⁺ and 4.9 min for In³⁺. The slow reaction time onset could be the result of a low concentration of catalytically active Al³⁺ cations in the precursor solution which would need to build up in the reaction solution before the metal catalyzed esterification rate could be observed. This hypothesis is also predicated on the idea that a small amount of catalyst could maintain a high esterification rate.

Although we do not have mol% dependent data for Al³⁺, we do have such data in the case of Ga³⁺. Here, the esterification rate was found to increase with mol% catalyst; however, the TON decreased due to the fact that [Ester]_{final} did not increase at the same rate as mol%. This observation suggests that only a small fraction of Ga³⁺ cations are driving the esterification reaction. Control experiments performed in which 100 mol% Ga³⁺ was present in the absence of Cu²⁺-O₂CR, the esterification rate was found to be 23 mM min⁻¹ and [Ester]_{final} = 270 mM. This equates to a TON of 2.3. The low TON is the result of [Ester]_{final} being roughly equal to that observed for 5–10 mol%

Ga^{3+} while the amount of catalyst was 10-20 times larger. One obvious reason for this is that a significant fraction of Ga^{3+} -OH species produced from each esterification cycle may undergo condensation with other Ga^{3+} -OH species to produce $\gamma\text{-Ga}_2\text{O}_3$. The condensation reaction would thus remove Ga^{3+} from the catalytic cycle and result in a lower amount of active catalysts. The same analysis can be performed with the 100 mol% In^{3+} condition in the absence of Cu^{2+} - O_2CR , resulting in an esterification rate of 19 mM min^{-1} , $[\text{Ester}]_{\text{final}} = 287 \text{ mM}$, and $\text{TON} = 2.6$.

The decrease in TON when going from 1 to 10 mol% Ga^{3+} may also be explained by competitive condensation which does not result in solid formation. Group 13 metals in aqueous solution are known to hydrolyze water to form μ -OH clusters.²⁹⁻³¹ When carboxylate ligands (*e.g.* acetate) are present, these clusters can also contain bridged carboxylates. In the case of Ga^{3+} and In^{3+} , oligomer chains of acetate ligands and metal cations have even been observed. It is therefore possible that μ -OH and μ -O coordinated Ga^{3+} clusters could result from condensation as the mol% is increased. This would thus lower the concentration of active Ga^{3+} cations for esterification. Notably, nucleation theory requires a critical concentration of monomers to be present in solution before nucleation may begin.⁴ Below this threshold, the coalescence of monomers into larger clusters is thought to occur but that such structures are unstable and dissolve back into monomer units. Given the established literature of group 13 clusters with μ -OH and μ -O ligands, we believe these species may be long lived during the catalytic cycle. In fact, the formation of trinuclear μ -O clusters in the synthesis of Fe_2O_3 with the continuous-injection method have been observed and used to explain the continuous growth of NCs.¹²

Based on the metrics presented for esterification catalysis, In^{3+} appears to be comparable with Ga^{3+} , however, a clear distinction is made between the morphology and size of the resulting Cu_2O NCs. In the case of In^{3+} , NCs with diameters $\geq 85 \text{ nm}$ were produced for all mol% conditions with spherical morphologies and a small degree of faceting. In the case of Ga^{3+} , resulting NCs were notably smaller ($\leq 72 \text{ nm}$) and displayed a distinct cubic morphology across all mol% conditions. We believe the origin for this result must be related to the inherent reactivity of each metal towards esterification and transmetallation. **Figure 7** shows FTIR ΔAbs spectra in the C=O region for 100 mol% Ga^{3+} and In^{3+} injections in the absence of Cu^{2+} - O_2CR . While both metals catalyze esterification equally well, there is a notable difference in the observed absorbance features in the range of $1650 - 1500 \text{ cm}^{-1}$. This region displays peaks associated with the C=O bond of the M^{3+} bound oleate ligand. Interestingly, when the Ga^{3+} - O_2CR was injected into oleyl alcohol at $200 \text{ }^\circ\text{C}$,

the precursor peak at 1563 cm^{-1} never grew in substantially during the reaction. In contrast, the $\text{In}^{3+}\text{-O}_2\text{CR}$ peak grew in markedly during the injection period before decaying away upon condensation to form In_2O_3 . Despite the $\text{Ga}^{3+}\text{-O}_2\text{CR}$ peak not being significantly present during the catalytic reaction, nanocrystalline Ga_2O_3 was still produced (**Figure S4**).

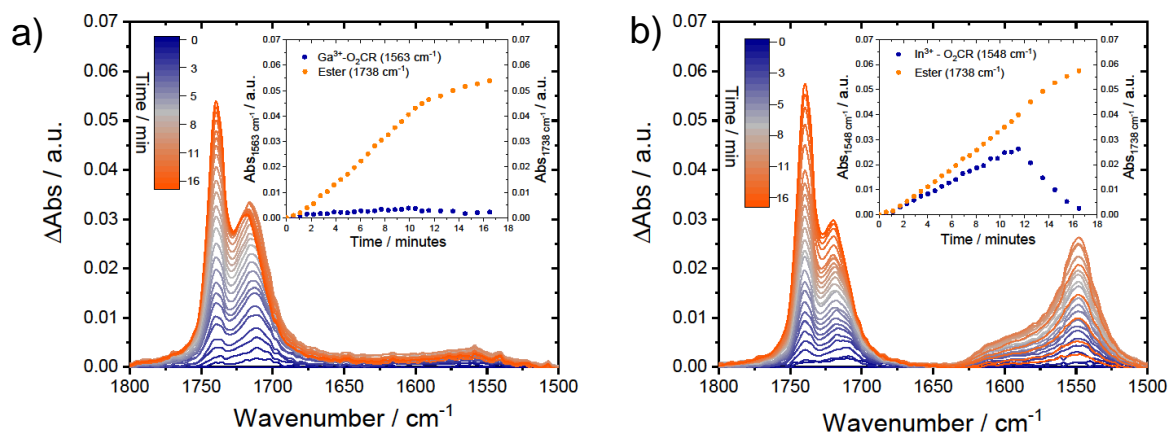


Figure 7. FTIR ΔAbs spectra for continuous-injection of 100 mol% a) $\text{Ga}^{3+}\text{-O}_2\text{CR}$ and b) $\text{In}^{3+}\text{-O}_2\text{CR}$ into oleyl alcohol at $200\text{ }^\circ\text{C}$ under N_2 . Insets for each figure show the precursor peak absorbance for $\text{M}^{3+}\text{-O}_2\text{CR}$ and oleyl oleate ester measured over the course of the reaction.

The absence of a precursor peak in the case of Ga^{3+} may be related to its ability to undergo condensation reactions to form $\mu\text{-OH}$ clusters. As discussed above, the mol% dependence for Ga^{3+} suggests that only a small fraction of Ga^{3+} cations are needed to maintain high levels of esterification. Indeed, the esterification rate and $[\text{Ester}]_{\text{final}}$ observed for 100 mol% Ga^{3+} were on par with those observed for 1-5 mol% Ga^{3+} . The propensity to form clusters may also be linked to the kinetics for transmetallation between Ga^{3+} and Cu^+ , as transmetallation would necessarily involve the formation of a bimetallic $\mu\text{-OH}$ complex to facilitate -OH ligand transfer.

In the case of In^{3+} , the persistence of the $\text{In}^{3+}\text{-O}_2\text{CR}$ peak could indicate slower reactivity toward condensation than Ga^{3+} . Fortunately, In_2O_3 synthesis and In^{3+} reactivity has been studied heavily by the Hutchison group^{8,9,16,22} where one particular study focused^{8,9,16,22} on the impact of temperature and injection rate on $\text{In}^{3+}\text{-O}_2\text{CR}$ precursor reactivity and the resulting morphology of In_2O_3 nanocrystals.³² They show that at lower temperatures and/or fast injection rates the $\text{In}^{3+}\text{-OH}$ monomers are slower to react, causing branched nanocrystals to form, as opposed to at high temperatures and slower injection rates where spherical particles are observed. Our reaction

conditions produced branched nanocrystals (**Figure S25**), which Plummer *et al.* state is related to long-lived In^{3+} -OH monomers in solution. Such long lifetimes would imply slow kinetics for condensation and thus transmetallation to Cu^+ .

Further evidence for the hypothesis of faster transmetallation kinetics for Ga^{3+} than In^{3+} can be found in the comparison of the 5 mol% catalyst data shown in **Figure 6**. In the case of Ga^{3+} , the time points at which the Cu^{2+} -O₂CR precursor peak decreased, associated with Cu_2O NC formation, and the onset for M^{3+} catalyzed esterification occurred were found to be identical at 4.3 min. In the case of In^{3+} , however, the decrease in the precursor peak (5.5 min) occurred 1.4 min after the onset of esterification (4.9 min). This lag in precursor consumption is a clear indication of transmetallation limited formation of Cu^+ -OH monomers needed for Cu_2O formation. The rapid transmetallation of -OH ligands from Ga^{3+} -OH is therefore believed to be a significant factor in producing the cubic morphology observed for Cu_2O NCs.

Relevance to Metal Oxide Synthesis Many Cu_2O syntheses exist in the literature that give a variety of sizes and morphologies.³³⁻⁴⁵ Early synthesis of small Cu_2O nanocrystals was achieved by oxidizing Cu^0 nanoparticles to Cu_2O in air.⁴⁶ This was characterized by a shift in color from metallic red to green. The green color of oxidized Cu^0 nanoparticles has been attributed to a Cu^0 core that remains buried beneath a Cu_2O shell.²⁰ Interestingly, Cu_2O that is synthesized directly (*i.e.* from Cu^+ -OH monomers) is yellow/orange in color.^{20,38,47} In most cases, our synthesis produced Cu_2O exclusively and through a direct route, but in the case of high temperature or with > 5 mol% Al^{3+} we produced Cu^0 nanocrystals, a small fraction of which turn green after oxidation in air, consistent with the literature.

Other syntheses which produced Cu_2O directly produce particles that are several hundred nanometers to microns in size and show impressive control over particle morphology.^{37,40,45,48-52} The morphological change observed here with the addition of Ga^{3+} is consistent with the formation of nanocubes. In the literature, fast reactivity of precursors has been attributed with the cubic morphology whereas slower reactivity has resulted in octahedral NCs.⁴⁰ Only a few synthetic methods have been shown to produce small colloidal Cu_2O NCs.^{20,23,38,47} These colloidal particles are capped with a variety of ligands including phosphate, amines, and carboxylates. The use of oleic acid in the continuous-injection method is necessary for the esterification reaction, but we also believe that amines or thiols could better cap the Cu_2O NCs, preventing agglomeration and resulting in smaller particle size.^{53,54}

We note that a recent report by Kim *et al.* described the effect of nonincorporative cations such as Na⁺ and K⁺ on the synthesis of In₂O₃ NCs where size and shape were effectively tuned.¹¹ These results were explained based on the concentration of free and bound oleate ligands, affected by [Na⁺] and [K⁺], and their influence of surface capping. In the present case, Ga³⁺ may exhibit similar effects to result in the nanocubic morphology of Cu₂O; however, we also believe that the rates of esterification by Ga³⁺-O₂CR and transmetallation by Ga³⁺-OH play significant roles to determine morphology. To the best of our knowledge, this is the first report of a transmetallation mechanism for metal oxide synthesis. The observation of this mechanism in the present system relies on the competitive nature of metal catalyzed esterification and M-OH condensation reactions. Cu⁺ appears to catalyze esterification slowly but undergo rapid condensation when Cu⁺-OH monomers are formed. Ga³⁺ and In³⁺ possess fast catalysis for esterification while their condensation reactions can be inhibited through low mol% loadings. This sets up a reaction scheme where Cu⁺ is able to bypass the esterification route and accept -OH ligands from M³⁺-OH through transmetallation. This type of mechanism could unlock the ability to use metal cations which are not prone to catalyzing the esterification reaction on their own. Although the esterification method has been shown for a number of metals, some have shown resistance to this reactivity, including copper, silver, and antimony.⁸ Furthermore, the inclusion of catalytic amounts of Ga³⁺ or In³⁺ into precursor solutions with other metals which are able to catalyze the esterification reaction (*i.e.* Fe, Co, Mn) may produce new reactivity through a more rapid production of -OH ligands in solution.

The possibility of transmetallation between two metal centers during the synthesis of metal oxides could also open the door to the preparation of new ternary oxide materials. For this to be achieved, the production M₁-OH and M₂-OH species would need to occur on the same timeframe and kinetics for cross condensation (*i.e.* M₁-OH + M₂-OH → M₁-O-M₂ + H₂O) would need to be faster than the formation of their respective binary oxides. The transmetallation step could even serve as a “buffer” to balance the rates of M₁-OH and M₂-OH production by transferring -OH ligands to the metal with a slower esterification rate. Indeed, the synthesis of some ternary oxide materials have already been reported in the literature using the continuous-injection method. However, these examples have centered on the synthesis of doped In₂O₃^{9,16,22} where the dopant metal occupies the same coordination environment and atomic position as In³⁺. It is possible that transmetallation between metals plays a role in the synthetic mechanism for these materials but has not yet been identified. It remains to be seen if the continuous-injection method can be used to

produce ternary oxide materials where each metal occupies a unique coordination environment. Notably, the formation of ternary oxides does not occur for the present reaction conditions. Even in the case of 1:1 Cu¹⁺:M³⁺ (the ratio for delafossite)⁵⁵⁻⁵⁷ or 1:2 Cu²⁺:M³⁺ (the ratio for spinel)⁵⁸, Cu₂O is always the major product. This speaks to a kinetic mismatch between the formation of Cu⁺-OH and M³⁺-OH species during the reaction.

Conclusion

Here we have shown a unique synthetic route for producing Cu₂O NCs by the addition of group 13 Lewis acid catalysts to a continuous-injection methodology. The inclusion of these catalysts are found to enhance the reaction efficiency of copper ions toward inclusion in Cu₂O NCs and result in higher production of M³⁺-OH species through esterification catalysis. Detailed time-dependent spectroscopic analysis reveals a unique transmetallation step between M³⁺-OH species and Cu⁺-O₂CR to generate Cu⁺-OH monomers. This step allows Cu⁺ to bypass the typical esterification route for generation of Cu⁺-OH and results in rapid condensation to form Cu₂O NCs. Of the group 13 metals, we find that Ga³⁺ exhibits our “goldilocks” reactivity, resulting in the smallest NCs and a distinctive cubic morphology. The use of Lewis acids in this reaction scheme could allow for a greater versatility in binary and ternary metal oxide formation. Further investigation of different metal-oleates and their reactivity with the continuous-injection method could allow for new syntheses to be developed for a wide variety of metal oxides.

Supporting Information

PXRD, SEM, TEM, EDS, UV-visible absorbance, and FTIR data.

Author Information

Corresponding Author

*farnum@auburn.edu

Notes

The authors declare no competing financial interests.

Acknowledgements

The authors acknowledge support from the National Science Foundation, Division of Materials Research and EPSCoR through grant 1809847. A.R.C.B. acknowledges support from the Alabama Graduate Research Scholars Program funded through Alabama Commission for Higher Education and administered by Alabama EPSCoR. N.G. acknowledges support from an Undergraduate Research Fellowship awarded through the Office of Undergraduate Research at Auburn University. PXRD measurements were collected on a Rigaku SmartLab funded through the National Science Foundation, Division of Materials Research, Major Research Instrumentation program under grant 2018794. The authors also thank Dr. Amar Kumbhar of the Chapel Hill Analytical and Nanofabrication Laboratory for assistance in collecting SEM, TEM, and EDS data.

References

- (1) Cargnello, M. Colloidal Nanocrystals as Building Blocks for Well-Defined Heterogeneous Catalysts. *Chem. Mater.* **2019**, *31* (3), 576–596. <https://doi.org/10.1021/acs.chemmater.8b04533>.
- (2) Yin, Y.; Alivisatos, A. P. Colloidal Nanocrystal Synthesis and the Organic–Inorganic Interface. *Nature* **2005**, *437* (7059), 664–670. <https://doi.org/10.1038/nature04165>.
- (3) E. Cloud, J.; S. Yoder, T.; K. Harvey, N.; Snow, K.; Yang, Y. A Simple and Generic Approach for Synthesizing Colloidal Metal and Metal Oxide Nanocrystals. *Nanoscale* **2013**, *5* (16), 7368–7378. <https://doi.org/10.1039/C3NR02404K>.
- (4) van Embden, J.; Chesman, A. S. R.; Jasieniak, J. J. The Heat-Up Synthesis of Colloidal Nanocrystals. *Chem. Mater.* **2015**, *27* (7), 2246–2285. <https://doi.org/10.1021/cm5028964>.
- (5) Agrawal, A.; Cho, S. H.; Zandi, O.; Ghosh, S.; Johns, R. W.; Milliron, D. J. Localized Surface Plasmon Resonance in Semiconductor Nanocrystals. *Chem. Rev.* **2018**, *118* (6), 3121–3207. <https://doi.org/10.1021/acs.chemrev.7b00613>.
- (6) LaMer, V. K.; Dinegar, R. H. Theory, Production and Mechanism of Formation of Monodispersed Hydrosols. *J. Am. Chem. Soc.* **1950**, *72* (11), 4847–4854. <https://doi.org/10.1021/ja01167a001>.
- (7) Wall, M. A.; Cossairt, B. M.; Liu, J. T. C. Reaction-Driven Nucleation Theory. *J. Phys. Chem. C* **2018**, *122* (17), 9671–9679. <https://doi.org/10.1021/acs.jpcc.8b01368>.
- (8) Ito, D.; Yokoyama, S.; Zaikova, T.; Masuko, K.; Hutchison, J. E. Synthesis of Ligand-Stabilized Metal Oxide Nanocrystals and Epitaxial Core/Shell Nanocrystals via a Lower-Temperature Esterification Process. *ACS Nano* **2014**, *8* (1), 64–75. <https://doi.org/10.1021/nn401888h>.
- (9) Jansons, A. W.; Hutchison, J. E. Continuous Growth of Metal Oxide Nanocrystals: Enhanced Control of Nanocrystal Size and Radial Dopant Distribution. *ACS Nano* **2016**, *10* (7), 6942–6951. <https://doi.org/10.1021/acs.nano.6b02796>.
- (10) Jansons, A. W.; Plummer, L. K.; Hutchison, J. E. Living Nanocrystals. *Chem. Mater.* **2017**, *29* (13), 5415–5425. <https://doi.org/10.1021/acs.chemmater.7b00899>.
- (11) Kim, K.; Reimnitz, L. C.; Cho, S. H.; Noh, J.; Dong, Z.; Gibbs, S. L.; Korgel, B. A.; Milliron, D. J. Effect of Nonincorporative Cations on the Size and Shape of Indium Oxide Nanocrystals. *Chem. Mater.* **2020**, *32* (21), 9347–9354. <https://doi.org/10.1021/acs.chemmater.0c03281>.
- (12) Chang, H.; Kim, B. H.; Jeong, H. Y.; Moon, J. H.; Park, M.; Shin, K.; Chae, S. I.; Lee, J.; Kang, T.; Choi, B. K.; Yang, J.; Bootharaju, M. S.; Song, H.; An, S. H.; Park, K. M.; Oh, J. Y.; Lee, H.; Kim, M. S.; Park, J.; Hyeon, T. Molecular-Level Understanding of Continuous Growth from Iron-Oxo Clusters to Iron Oxide Nanoparticles. *J. Am. Chem. Soc.* **2019**, *141* (17), 7037–7045. <https://doi.org/10.1021/jacs.9b01670>.
- (13) Plummer, L. K.; Hutchison, J. E. Understanding the Effects of Iron Precursor Ligation and Oxidation State Leads to Improved Synthetic Control for Spinel Iron Oxide Nanocrystals. *Inorg. Chem.* **2020**, *59* (20), 15074–15087. <https://doi.org/10.1021/acs.inorgchem.0c02040>.
- (14) Cooper, S. R.; Plummer, L. K.; Cosby, A. G.; Lenox, P.; Jander, A.; Dhagat, P.; Hutchison, J. E. Insights into the Magnetic Properties of Sub-10 Nm Iron Oxide Nanocrystals through the Use of a Continuous Growth Synthesis. *Chem. Mater.* **2018**, *30* (17), 6053–6062. <https://doi.org/10.1021/acs.chemmater.8b02389>.
- (15) Wainer, P.; Kendall, O.; Lamb, A.; Barrow, S. J.; Tricoli, A.; Gómez, D. E.; van Embden, J.; Della Gaspera, E. Continuous Growth Synthesis of Zinc Oxide Nanocrystals with Tunable Size and Doping. *Chem. Mater.* **2019**, *31* (23), 9604–9613. <https://doi.org/10.1021/acs.chemmater.9b02655>.
- (16) Jansons, A. W.; Koskela, K. M.; Crockett, B. M.; Hutchison, J. E. Transition Metal-Doped Metal Oxide Nanocrystals: Efficient Substitutional Doping through a Continuous Growth Process. *Chem. Mater.* **2017**, *29* (19), 8167–8176. <https://doi.org/10.1021/acs.chemmater.7b02176>.
- (17) Li, X.; Shen, H.; Niu, J.; Li, S.; Zhang, Y.; Wang, H.; Li, L. S. Columnar Self-Assembly of Cu₂S Hexagonal Nanoplates Induced by Tin(IV)–X Complex as Inorganic Surface Ligand. *J. Am. Chem. Soc.* **2010**, *132* (37), 12778–12779. <https://doi.org/10.1021/ja103955s>.

- (18) Yi, L.; Gao, M. From Ultrathin Two-Dimensional Djurleite Nanosheets to One-Dimensional Nanorods Comprised of Djurleite Nanoplates: Synthesis, Characterization, and Formation Mechanism. *Cryst. Growth Des.* **2011**, *11* (4), 1109–1116. <https://doi.org/10.1021/cg101322s>.
- (19) Machani, T.; Rossi, D. P.; Golden, B. J.; Jones, E. C.; Lotfipour, M.; Plass, K. E. Synthesis of Monoclinic and Tetragonal Chalcocite Nanoparticles by Iron-Induced Stabilization. *Chem. Mater.* **2011**, *23* (24), 5491–5495. <https://doi.org/10.1021/cm2022196>.
- (20) Pike, S. D.; White, E. R.; Regoutz, A.; Sammy, N.; Payne, D. J.; Williams, C. K.; Shaffer, M. S. P. Reversible Redox Cycling of Well-Defined, Ultrasmall Cu/Cu₂O Nanoparticles. *ACS Nano* **2017**, *11* (3), 2714–2723. <https://doi.org/10.1021/acsnano.6b07694>.
- (21) Singhal, A.; Pai, M. R.; Rao, R.; Pillai, K. T.; Lieberwirth, I.; Tyagi, A. K. Copper(I) Oxide Nanocrystals – One Step Synthesis, Characterization, Formation Mechanism, and Photocatalytic Properties. *Eur. J. Inorg. Chem.* **2013**, *2013* (14), 2640–2651. <https://doi.org/10.1002/ejic.201201382>.
- (22) Crockett, B. M.; Jansons, A. W.; Koskela, K. M.; Sharps, M. C.; Johnson, D. W.; Hutchison, J. E. Influence of Nanocrystal Size on the Optoelectronic Properties of Thin, Solution-Cast Sn-Doped In₂O₃ Films. *Chem. Mater.* **2019**, *31* (9), 3370–3380. <https://doi.org/10.1021/acs.chemmater.9b00538>.
- (23) Tariq, M.; Koch, M. D.; Andrews, J. W.; Knowles, K. E. Correlation between Surface Chemistry and Optical Properties in Colloidal Cu₂O Nanoparticles. *J. Phys. Chem. C* **2020**, *124* (8), 4810–4819. <https://doi.org/10.1021/acs.jpcc.9b10753>.
- (24) Mamidi, N.; Manna, D. Zn(OTf)₂-Promoted Chemoselective Esterification of Hydroxyl Group Bearing Carboxylic Acids. *J. Org. Chem.* **2013**, *78* (6), 2386–2396. <https://doi.org/10.1021/jo302502r>.
- (25) Hou, X.; Qi, Y.; Qiao, X.; Wang, G.; Qin, Z.; Wang, J. Lewis Acid-Catalyzed Transesterification and Esterification of High Free Fatty Acid Oil in Subcritical Methanol. *Korean J. Chem. Eng.* **2007**, *24* (2), 311–313. <https://doi.org/10.1007/s11814-007-5052-x>.
- (26) Maki, T.; Ishihara, K.; Yamamoto, H. N-Alkyl-4-Boronopyridinium Halides versus Boric Acid as Catalysts for the Esterification of α -Hydroxycarboxylic Acids. *Org. Lett.* **2005**, *7* (22), 5047–5050. <https://doi.org/10.1021/ol052061d>.
- (27) Ishihara, K.; Nakayama, M.; Ohara, S.; Yamamoto, H. Direct Ester Condensation from a 1:1 Mixture of Carboxylic Acids and Alcohols Catalyzed by Hafnium(IV) or Zirconium(IV) Salts. *Tetrahedron* **2002**, *58* (41), 8179–8188. [https://doi.org/10.1016/S0040-4020\(02\)00966-3](https://doi.org/10.1016/S0040-4020(02)00966-3).
- (28) Bentley, J. N.; Elgadi, S. A.; Gaffen, J. R.; Demay-Drouhard, P.; Baumgartner, T.; Caputo, C. B. Fluorescent Lewis Adducts: A Practical Guide to Relative Lewis Acidity. *Organometallics* **2020**. <https://doi.org/10.1021/acs.organomet.0c00389>.
- (29) Kamunde-Devonish, M. K.; Fast, D. B.; Mensinger, Z. L.; Gatlin, J. T.; Zakharov, L. N.; Dolgos, M. R.; Johnson, D. W. Synthesis and Solid-State Structural Characterization of a Series of Aqueous Heterometallic Tridecameric Group 13 Clusters. *Inorg. Chem.* **2015**, *54* (8), 3913–3920. <https://doi.org/10.1021/acs.inorgchem.5b00097>.
- (30) Mensinger, Z. L.; Zakharov, L. N.; Johnson, D. W. Synthesis and Crystallization of Infinite Indium and Gallium Acetate 1D Chain Structures and Concomitant Ethyl Acetate Hydrolysis. *Inorg. Chem.* **2009**, *48* (8), 3505–3507. <https://doi.org/10.1021/ic9000945>.
- (31) Clausén, M.; Öhman, L.-O.; Kubicki, J. D.; Persson, P. Characterisation of Gallium(III)-Acetate Complexes in Aqueous Solution: A Potentiometric, EXAFS, IR and Molecular Orbital Modelling Study. *J. Chem. Soc. Dalton Trans.* **2002**, No. 12, 2559–2564. <https://doi.org/10.1039/B111408E>.
- (32) Plummer, L. K.; Crockett, B. M.; Pennel, M. L.; Jansons, A. W.; Koskela, K. M.; Hutchison, J. E. Influence of Monomer Flux and Temperature on Morphology of Indium Oxide Nanocrystals during a Continuous Growth Synthesis. *Chem. Mater.* **2019**, *31* (18), 7638–7649. <https://doi.org/10.1021/acs.chemmater.9b02467>.
- (33) Thoka, S.; Lee, A.-T.; Huang, M. H. Scalable Synthesis of Size-Tunable Small Cu₂O Nanocubes and Octahedra for Facet-Dependent Optical Characterization and Pseudomorphic Conversion to Cu

- Nanocrystals. *ACS Sustain. Chem. Eng.* **2019**, *7* (12), 10467–10476. <https://doi.org/10.1021/acssuschemeng.9b00844>.
- (34) Mukherjee, I.; Das, S. K.; Jena, B. K.; Saha, R.; Chatterjee, S. Dissimilitude Behaviour of Cu₂O Nano-Octahedra and Nano-Cubes towards Photo- and Electrocatalytic Activities. *New J. Chem.* **2018**, *42* (5), 3692–3702. <https://doi.org/10.1039/C7NJ04474G>.
- (35) Zhang, X.; Zhang, Y.; Huang, H.; Cai, J.; Ding, K.; Lin, S. Electrochemical Fabrication of Shape-Controlled Cu₂O with Spheres, Octahedrons and Truncated Octahedrons and Their Electrocatalysis for ORR. *New J. Chem.* **2017**, *42* (1), 458–464. <https://doi.org/10.1039/C7NJ04200K>.
- (36) Wang, Q.; Kuang, Q.; Wang, K.; Wang, X.; Xie, Z. A Surfactant Free Synthesis and Formation Mechanism of Hollow Cu₂O Nanocubes Using Cl⁻ Ions as the Morphology Regulator. *RSC Adv.* **2015**, *5* (75), 61421–61425. <https://doi.org/10.1039/C5RA08988C>.
- (37) Susman, M. D.; Feldman, Y.; Vaskevich, A.; Rubinstein, I. Chemical Deposition of Cu₂O Nanocrystals with Precise Morphology Control. *ACS Nano* **2014**, *8* (1), 162–174. <https://doi.org/10.1021/nn405891g>.
- (38) Paolella, A.; Brescia, R.; Prato, M.; Povia, M.; Marras, S.; De Trizio, L.; Falqui, A.; Manna, L.; George, C. Colloidal Synthesis of Cuprite (Cu₂O) Octahedral Nanocrystals and Their Electrochemical Lithiation. *ACS Appl. Mater. Interfaces* **2013**, *5* (7), 2745–2751. <https://doi.org/10.1021/am4004073>.
- (39) Li, Q.; Xu, P.; Zhang, B.; Tsai, H.; Zheng, S.; Wu, G.; Wang, H.-L. Structure-Dependent Electrocatalytic Properties of Cu₂O Nanocrystals for Oxygen Reduction Reaction. *J. Phys. Chem. C* **2013**, *117* (27), 13872–13878. <https://doi.org/10.1021/jp403655y>.
- (40) Huang, W.-C.; Lyu, L.-M.; Yang, Y.-C.; Huang, M. H. Synthesis of Cu₂O Nanocrystals from Cubic to Rhombic Dodecahedral Structures and Their Comparative Photocatalytic Activity. *J. Am. Chem. Soc.* **2012**, *134* (2), 1261–1267. <https://doi.org/10.1021/ja209662v>.
- (41) Hua, Q.; Shang, D.; Zhang, W.; Chen, K.; Chang, S.; Ma, Y.; Jiang, Z.; Yang, J.; Huang, W. Morphological Evolution of Cu₂O Nanocrystals in an Acid Solution: Stability of Different Crystal Planes. *Langmuir* **2011**, *27* (2), 665–671. <https://doi.org/10.1021/la104475s>.
- (42) Yao, K. X.; Yin, X. M.; Wang, T. H.; Zeng, H. C. Synthesis, Self-Assembly, Disassembly, and Reassembly of Two Types of Cu₂O Nanocrystals Unifaceted with {001} or {110} Planes. *J. Am. Chem. Soc.* **2010**, *132* (17), 6131–6144. <https://doi.org/10.1021/ja100151f>.
- (43) Sun, S.; Zhou, F.; Wang, L.; Song, X.; Yang, Z. Template-Free Synthesis of Well-Defined Truncated Edge Polyhedral Cu₂O Architectures. *Cryst. Growth Des.* **2010**, *10* (2), 541–547. <https://doi.org/10.1021/cg900756u>.
- (44) Sui, Y.; Fu, W.; Yang, H.; Zeng, Y.; Zhang, Y.; Zhao, Q.; Li, Y.; Zhou, X.; Leng, Y.; Li, M.; Zou, G. Low Temperature Synthesis of Cu₂O Crystals: Shape Evolution and Growth Mechanism. *Cryst. Growth Des.* **2010**, *10* (1), 99–108. <https://doi.org/10.1021/cg900437x>.
- (45) Kuo, C.-H.; Huang, M. H. Morphologically Controlled Synthesis of Cu₂O Nanocrystals and Their Properties. *Nano Today* **2010**, *5* (2), 106–116. <https://doi.org/10.1016/j.nantod.2010.02.001>.
- (46) Yin, M.; Wu, C.-K.; Lou, Y.; Burda, C.; Koberstein, J. T.; Zhu, Y.; O'Brien, S. Copper Oxide Nanocrystals. *J. Am. Chem. Soc.* **2005**, *127* (26), 9506–9511. <https://doi.org/10.1021/ja050006u>.
- (47) Yuan, X.; Yuan, H.; Ye, L.; Hu, J.; Xu, Y.; Li, P. Ultrasmall Cu₂O Nanocrystals: Facile Synthesis, Controllable Assembly and Photocatalytic Properties. *RSC Adv.* **2015**, *5* (53), 42855–42860. <https://doi.org/10.1039/C5RA06141E>.
- (48) Nikam, A. V.; Arulkashmir, A.; Krishnamoorthy, K.; Kulkarni, A. A.; Prasad, B. L. V. PH-Dependent Single-Step Rapid Synthesis of CuO and Cu₂O Nanoparticles from the Same Precursor. *Cryst. Growth Des.* **2014**, *14* (9), 4329–4334. <https://doi.org/10.1021/cg500394p>.
- (49) Shi, H.; Yu, K.; Sun, F.; Zhu, Z. Controllable Synthesis of Novel Cu₂O Micro/Nano-Crystals and Their Photoluminescence, Photocatalytic and Field Emission Properties. *CrystEngComm* **2011**, *14* (1), 278–285. <https://doi.org/10.1039/C1CE05868A>.

- (50) Zhang, Y.; Deng, B.; Zhang, T.; Gao, D.; Xu, A.-W. Shape Effects of Cu₂O Polyhedral Microcrystals on Photocatalytic Activity. *J. Phys. Chem. C* **2010**, *114* (11), 5073–5079. <https://doi.org/10.1021/jp9110037>.
- (51) Luo, Y.; Li, S.; Ren, Q.; Liu, J.; Xing, L.; Wang, Y.; Yu, Y.; Jia, Z.; Li, J. Facile Synthesis of Flowerlike Cu₂O Nanoarchitectures by a Solution Phase Route. *Cryst. Growth Des.* **2007**, *7* (1), 87–92. <https://doi.org/10.1021/cg060491k>.
- (52) Kuo, C.-H.; Huang, M. H. Facile Synthesis of Cu₂O Nanocrystals with Systematic Shape Evolution from Cubic to Octahedral Structures. *J. Phys. Chem. C* **2008**, *112* (47), 18355–18360. <https://doi.org/10.1021/jp8060027>.
- (53) Kauffman, D. R.; Ohodnicki, P. R.; Kail, B. W.; Matranga, C. Selective Electrocatalytic Activity of Ligand Stabilized Copper Oxide Nanoparticles. *J. Phys. Chem. Lett.* **2011**, *2* (16), 2038–2043. <https://doi.org/10.1021/jz200850y>.
- (54) Oliva-Puigdomènech, A.; De Roo, J.; Kuhs, J.; Detavernier, C.; Martins, J. C.; Hens, Z. Ligand Binding to Copper Nanocrystals: Amines and Carboxylic Acids and the Role of Surface Oxides. *Chem. Mater.* **2019**, *31* (6), 2058–2067. <https://doi.org/10.1021/acs.chemmater.8b05107>.
- (55) Pamplin, B. R.; Kiyosawa, T.; Masumoto, K. Ternary Chalcopyrite Compounds. *Prog. Cryst. Growth Charact.* **1979**, *1* (4), 331–387. [https://doi.org/10.1016/0146-3535\(79\)90002-9](https://doi.org/10.1016/0146-3535(79)90002-9).
- (56) Kawazoe, H.; Yasukawa, M.; Hyodo, H.; Kurita, M.; Yanagi, H.; Hosono, H. P-Type Electrical Conduction in Transparent Thin Films of CuAlO₂. *Nature* **1997**, *389* (6654), 939–942. <https://doi.org/10.1038/40087>.
- (57) Omata, T.; Nagatani, H.; Suzuki, I.; Kita, M.; Yanagi, H.; Ohashi, N. Wurtzite CuGaO₂: A New Direct and Narrow Band Gap Oxide Semiconductor Applicable as a Solar Cell Absorber. *J. Am. Chem. Soc.* **2014**, *136* (9), 3378–3381. <https://doi.org/10.1021/ja501614n>.
- (58) Conrad, F.; Massue, C.; Kühn, S.; Kunkes, E.; Girgsdies, F.; Kasatkin, I.; Zhang, B.; Friedrich, M.; Luo, Y.; Armbrüster, M.; R. Patzke, G.; Behrens, M. Microwave-Hydrothermal Synthesis and Characterization of Nanostructured Copper Substituted ZnM₂O₄ (M = Al, Ga) Spinel as Precursors for Thermally Stable Cu Catalysts. *Nanoscale* **2012**, *4* (6), 2018–2028. <https://doi.org/10.1039/C2NR11804A>.

Supporting Information

Group 13 Lewis Acid Catalyzed Synthesis of Cu₂O Nanoparticles via Hydroxide Transmetallation

Noah J. Gibson[†], Alexandria R. C. Bredar[†], Byron H. Farnum*

Department of Chemistry and Biochemistry

Auburn University, Auburn, AL 36849

*Corresponding Author: farnum@auburn.edu

Table of Contents

Figure S1. PXRD of Al ³⁺ , Ga ³⁺ , and In ³⁺ catalyzed Cu ₂ O reaction products	S-2
Figure S2. PXRD of reaction products at 200 °C and 215 °C	S-3
Figure S3. FTIR and UV-Vis of copper (I) vs copper (II) acetate	S-3
Figure S4. PXRD of 100% Ga ³⁺ and In ³⁺ injection reactions	S-4
Figure S5. SEM of 1, 5, and 15 mol% Al ³⁺ , Ga ³⁺ , and In ³⁺ reaction products	S-4
Figure S6. Histograms of 0-15 mol% Al ³⁺ , Ga ³⁺ , In ³⁺ synthesized NCs	S-5
Figure S7. TEM and EDS of 0 mol% catalyzed reaction	S-6
Figure S8. TEM and EDS of 1 mol% Ga ³⁺ catalyzed reaction	S-6
Figure S9. TEM and EDS of 5 mol% Ga ³⁺ catalyzed reaction	S-7
Figure S10. TEM and EDS of 10 mol% Ga ³⁺ catalyzed reaction	S-7
Figure S11. TEM and EDS of 15 mol% Ga ³⁺ catalyzed reaction	S-8
Figure S12. TEM and EDS of 1 mol% In ³⁺ catalyzed reaction	S-8
Figure S13. TEM and EDS of 5 mol% In ³⁺ catalyzed reaction	S-9
Figure S14. TEM and EDS of 10 mol% In ³⁺ catalyzed reaction	S-9
Figure S15. TEM and EDS of 15 mol% In ³⁺ catalyzed reaction	S-10
Figure S16. UV-visible absorption spectra and calibration curve of Cu ²⁺ -O ₂ CR	S-10
Figure S17. UV-visible absorption spectra of Al ³⁺ , Ga ³⁺ , and In ³⁺ catalyzed reactions	S-11
Figure S18. FTIR spectra of In ³⁺ and Al ³⁺ catalyzed reactions	S-11
Figure S19. FTIR spectra and calibration curve of oleic acid	S-12
Figure S20. FTIR spectra and calibration curve of Cu ²⁺ -O ₂ CR	S-13
Figure S21. FTIR ΔAbs spectra and time dependent plot of oleyl oleate ester	S-13
Figure S22. Time-dependent FTIR ΔAbs spectra for Al ³⁺ , Ga ³⁺ , and In ³⁺ catalyzed reactions	S-14
Figure S23. Time-dependent UV-vis absorption spectra for Al ³⁺ , Ga ³⁺ , and In ³⁺ catalyzed reactions	S-15
Figure S24. Al ³⁺ , Ga ³⁺ , and In ³⁺ 5 mol% control injections	S-16
Figure S25. TEM HAADF images of In ₂ O ₃ nanocrystals	S-16

Supporting Information

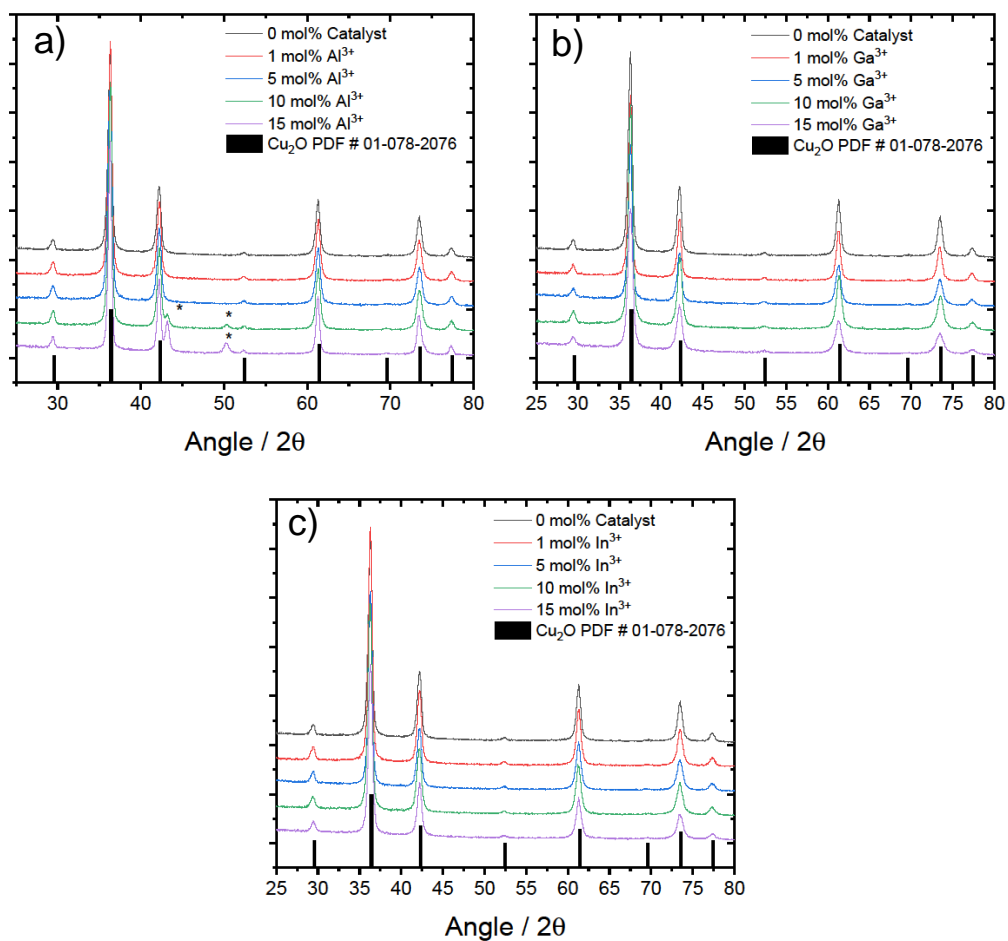


Figure S1. XRD of a) Al^{3+} , b) Ga^{3+} , and c) In^{3+} catalyzed Cu_2O . Asterisks (*) in Al^{3+} data refer to peaks associated with Cu^0 .

Supporting Information

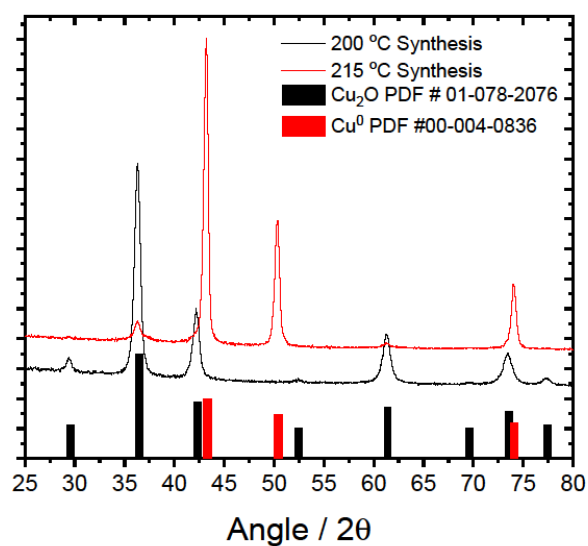


Figure S2. PXRD of reaction products at 200 °C and 215 °C.

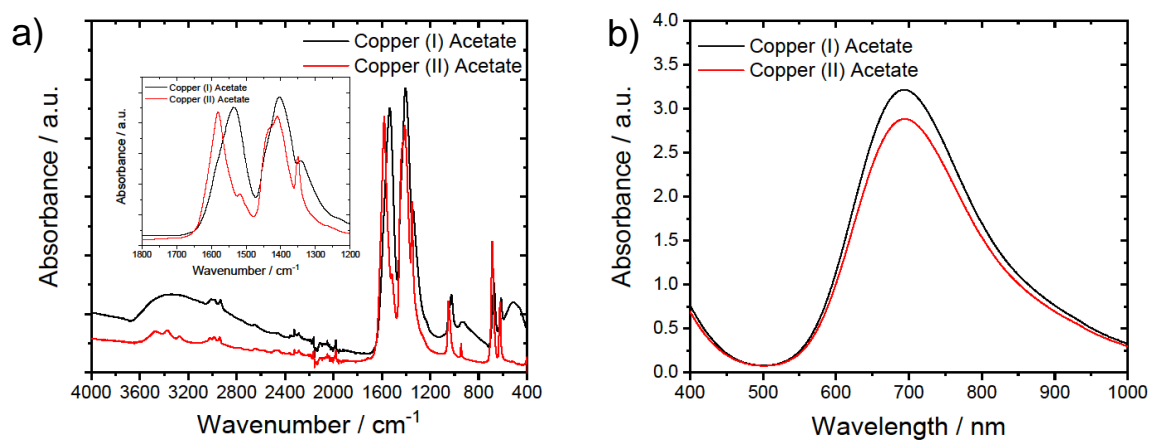


Figure S3. a) FTIR of copper (I) acetate and copper (II) acetate solids. b) UV-Vis of precursors synthesized from the exchange of copper (I) acetate and copper (II) acetate with oleic acid. Both solutions were made at 68 mM by dilution with oleyl alcohol.

Supporting Information

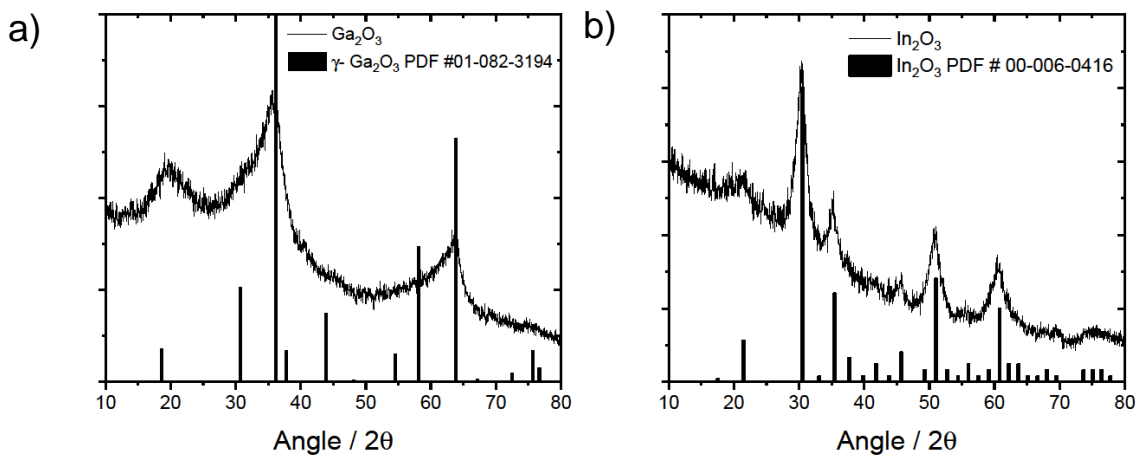


Figure S4. PXRD of a) γ - Ga_2O_3 and b) In_2O_3 synthesized via continuous-injection of 2 mmol of M^{3+} - O_2CR into oleyl alcohol at 200 °C under N_2 .

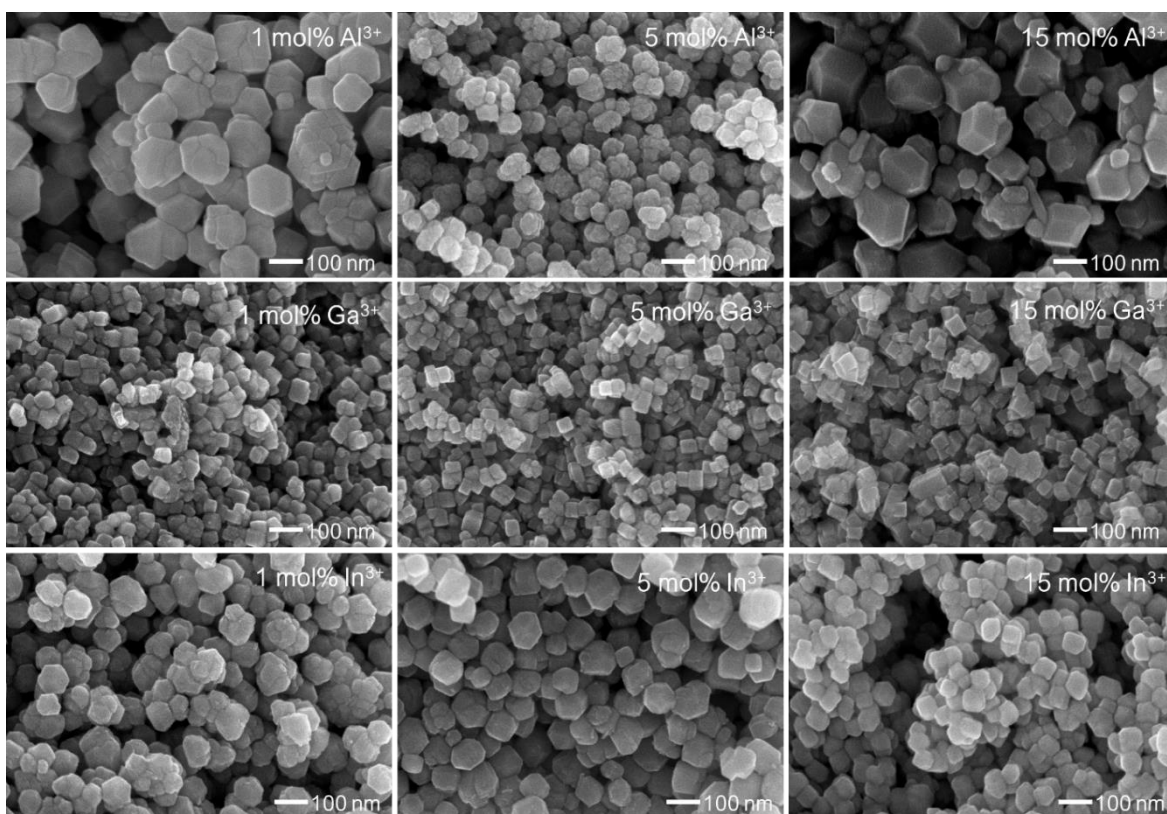


Figure S5. SEM of Cu_2O nanocrystals synthesized with 1, 5, and 15 mol% Al^{3+} , Ga^{3+} , and In^{3+} catalysts.

Supporting Information

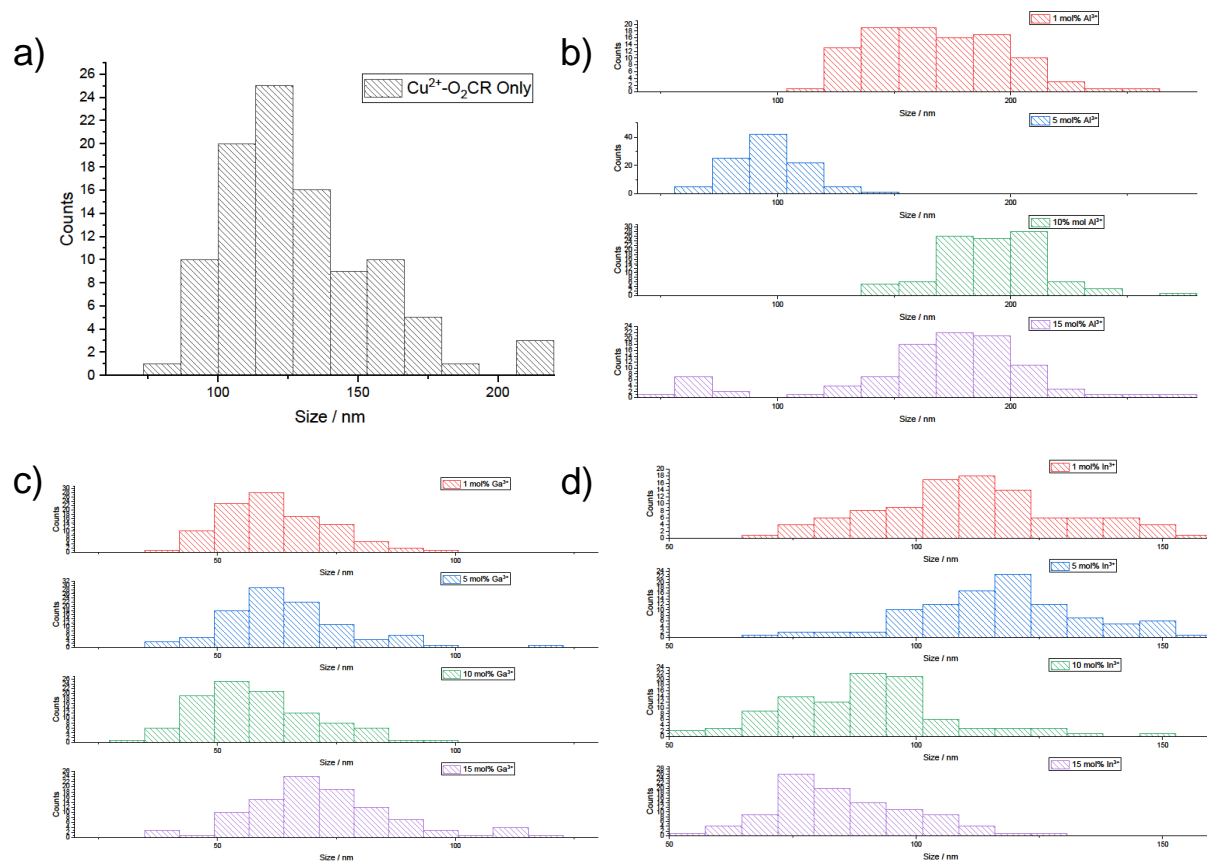


Figure S6. Histograms for a) Cu^{2+} - O_2CR only injection, b) 1-15 mol% Al^{3+} , c) 1-15 mol% Ga^{3+} , and d) 1-15 mol% In^{3+} . Size analysis was performed from SEM images.

Supporting Information

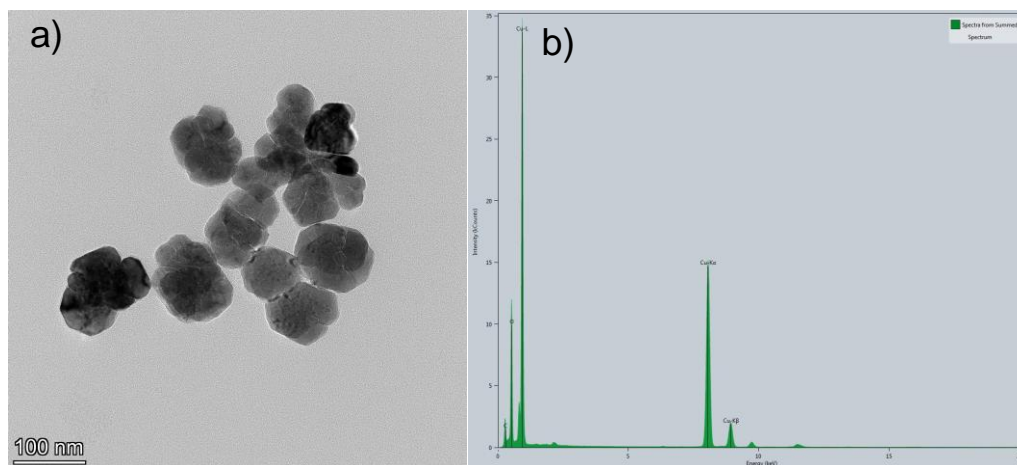


Figure S7. a) TEM and b) EDS of Cu^{2+} reaction with 0 mol% catalyst. Unlabeled peaks near 2, 9, and 12 keV are due to Au (TEM grid).

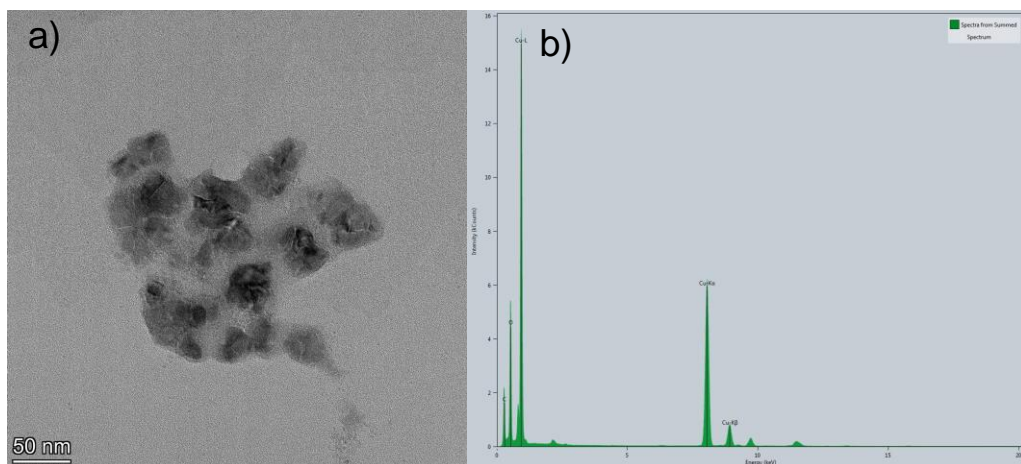


Figure S8. a) TEM and b) EDS of Cu^{2+} reaction with 1 mol% Ga^{3+} catalyst. Unlabeled peaks near 2, 9, and 12 keV are due to Au (TEM grid).

Supporting Information

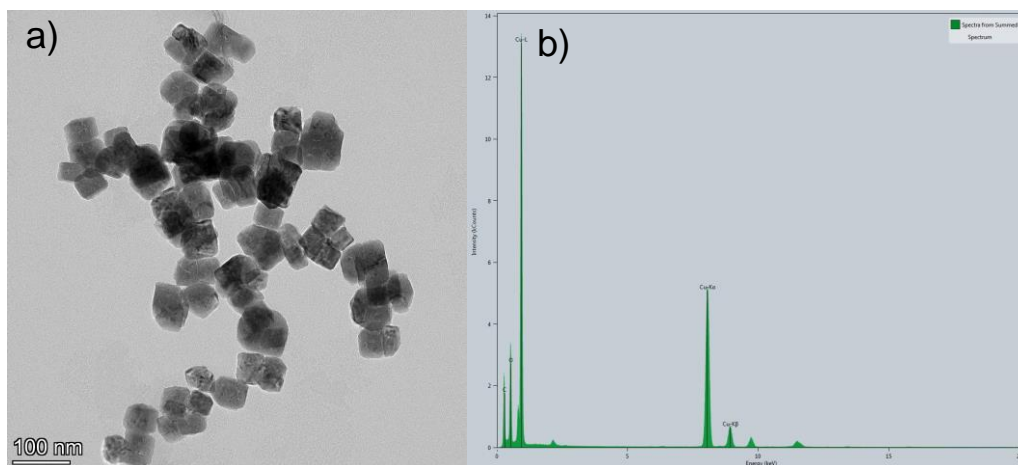


Figure S9. a) TEM and b) EDS of Cu^{2+} reaction with 5 mol% Ga^{3+} catalyst. Unlabeled peaks near 2, 9, and 12 keV are due to Au (TEM grid).

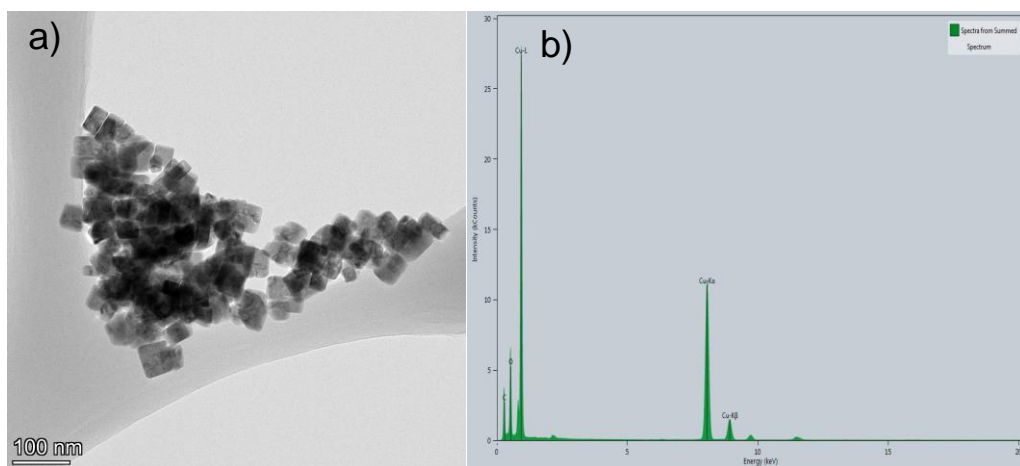


Figure S10. a) TEM and b) EDS of Cu^{2+} reaction with 10 mol% Ga^{3+} catalyst. Unlabeled peaks near 2, 9, and 12 keV are due to Au (TEM grid).

Supporting Information

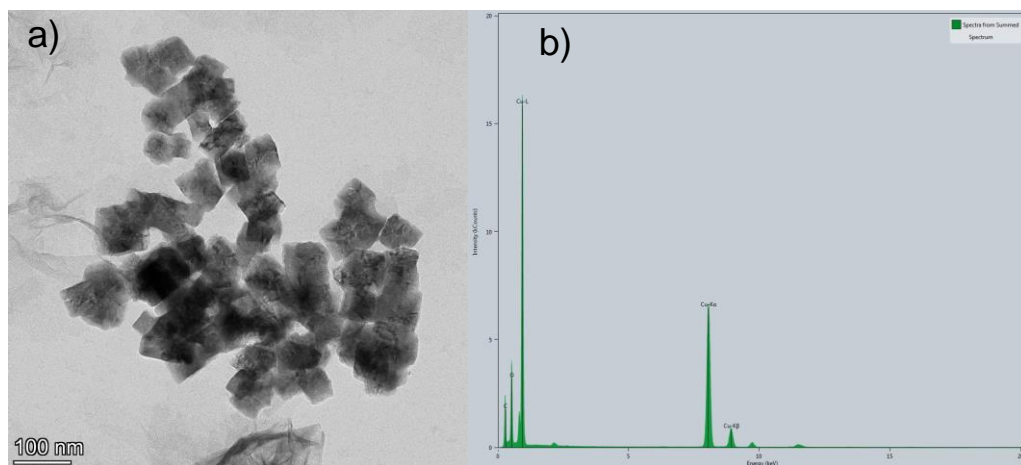


Figure S11. a) TEM and b) EDS of Cu^{2+} reaction with 15 mol% Ga^{3+} catalyst. Unlabeled peaks near 2, 9, and 12 keV are due to Au (TEM grid).

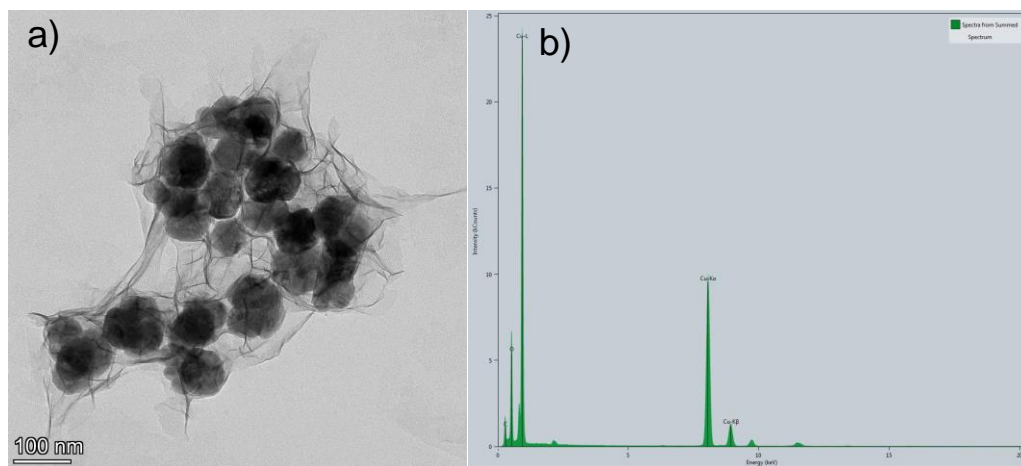


Figure S12. a) TEM and b) EDS of Cu^{2+} reaction with 1 mol% In^{3+} catalyst. Unlabeled peaks near 2, 9, and 12 keV are due to Au (TEM grid).

Supporting Information

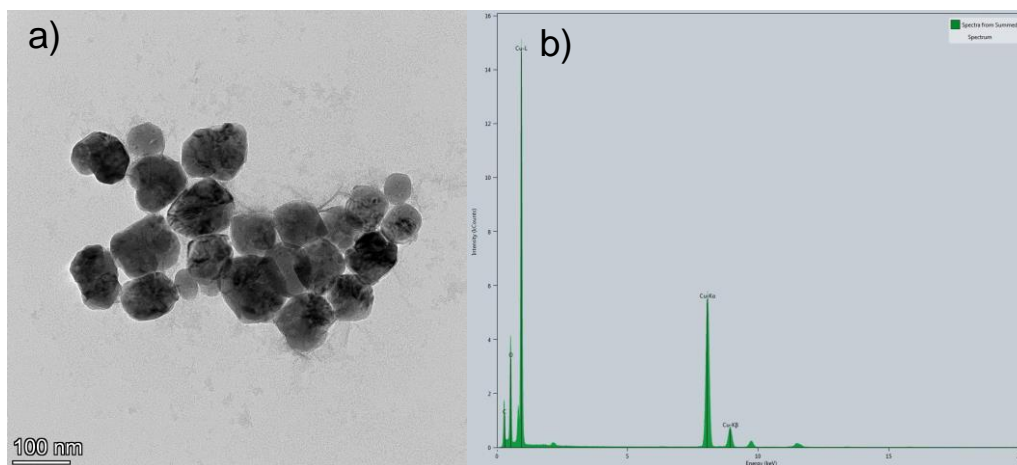


Figure S13. a) TEM and b) EDS of Cu^{2+} reaction with 5 mol% In^{3+} catalyst. Unlabeled peaks near 2, 9, and 12 keV are due to Au (TEM grid).

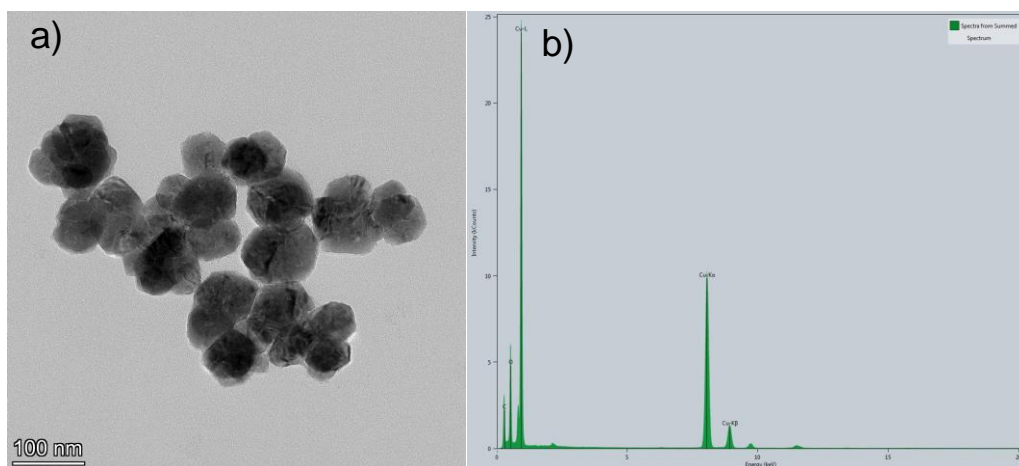


Figure S14. a) TEM and b) EDS of Cu^{2+} reaction with 10 mol% In^{3+} catalyst. Unlabeled peaks near 2, 9, and 12 keV are due to Au (TEM grid).

Supporting Information

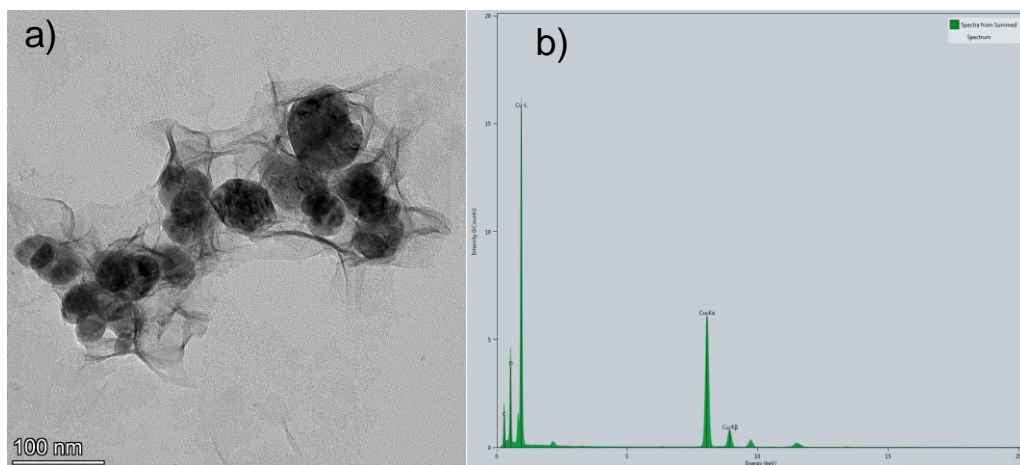


Figure S15. a) TEM and b) EDS of Cu^{2+} reaction with 15 mol% In^{3+} catalyst. Unlabeled peaks near 2, 9, and 12 keV are due to Au (TEM grid).

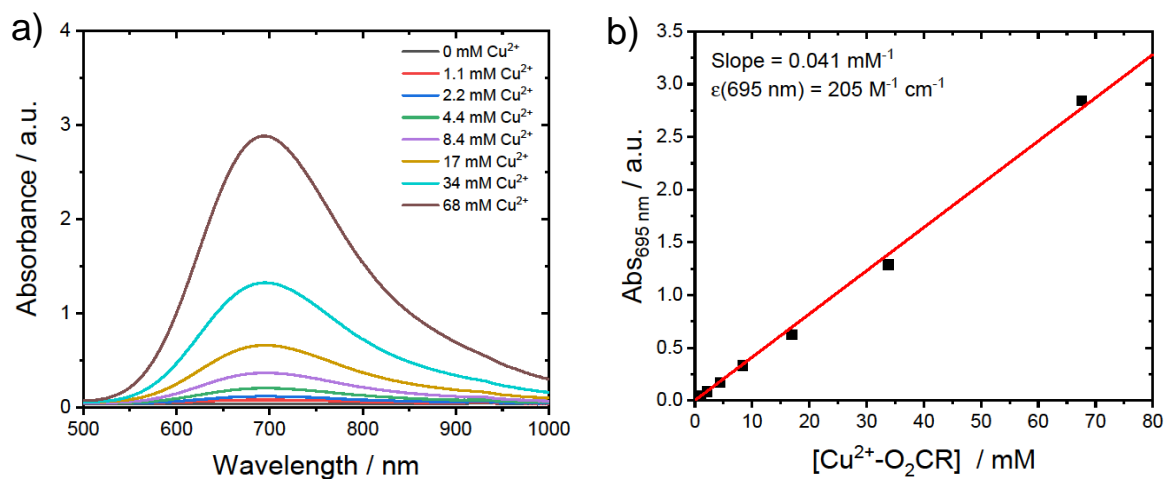


Figure S16. a) UV-visible absorbance spectra of Cu^{2+} - O_2CR precursor in oleyl alcohol at controlled concentrations collected in a 0.2 cm path length cuvette. b) Beer-Lambert plot for peak absorbance at 695 nm. Measured slope of 0.041 mM⁻¹ results in a calculated $\epsilon(695 \text{ nm}) = 205 \text{ M}^{-1} \text{ cm}^{-1}$.

Supporting Information

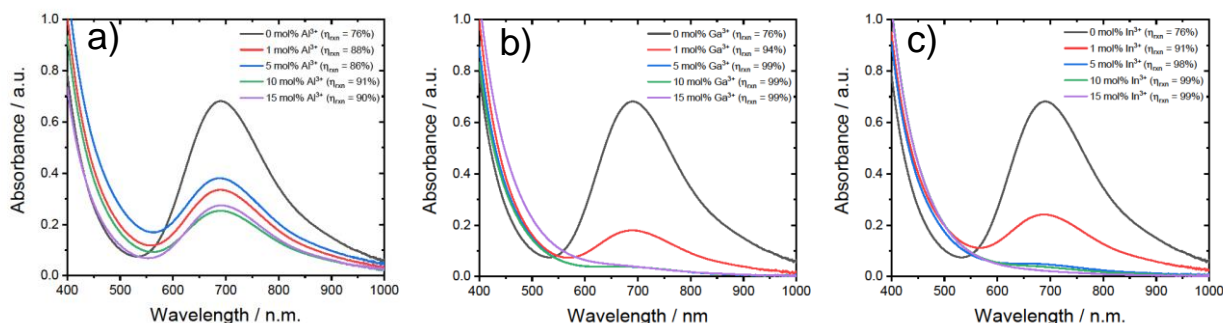


Figure S17. UV-visible absorbance spectra of post-reaction solutions for a) Al³⁺, b) Ga³⁺, and c) In³⁺ catalysts (0.2 cm path length). The peak at 695 nm is indicative of unreacted Cu²⁺-O₂CR precursor remaining in solution. Absorbance was corrected for oleyl alcohol with the reaction efficiency indicated in the legend ($\eta_{\text{rxn}} = 1 - [\text{Cu}^{2+}]_{\text{unreacted}}/[\text{Cu}^{2+}]_{\text{total}}$). [Cu²⁺] concentration calculated using $\epsilon_{695} = 205 \text{ M}^{-1} \text{ cm}^{-1}$ determined in **Figure S16**. [Cu²⁺]_{total} = 68 mM.

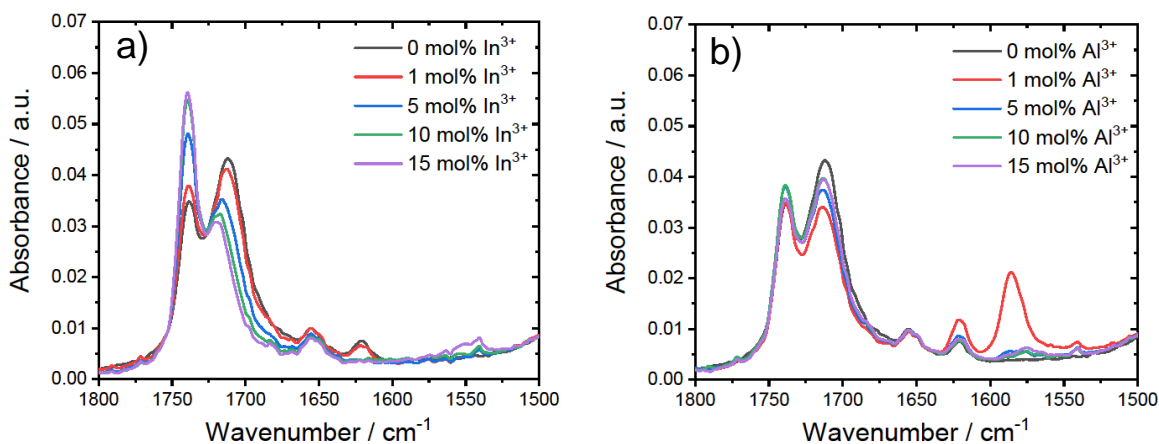


Figure S18: FTIR absorbance spectra of post-reaction solutions of a) In³⁺ and b) Al³⁺ catalyzed Cu₂O synthesis.

Supporting Information

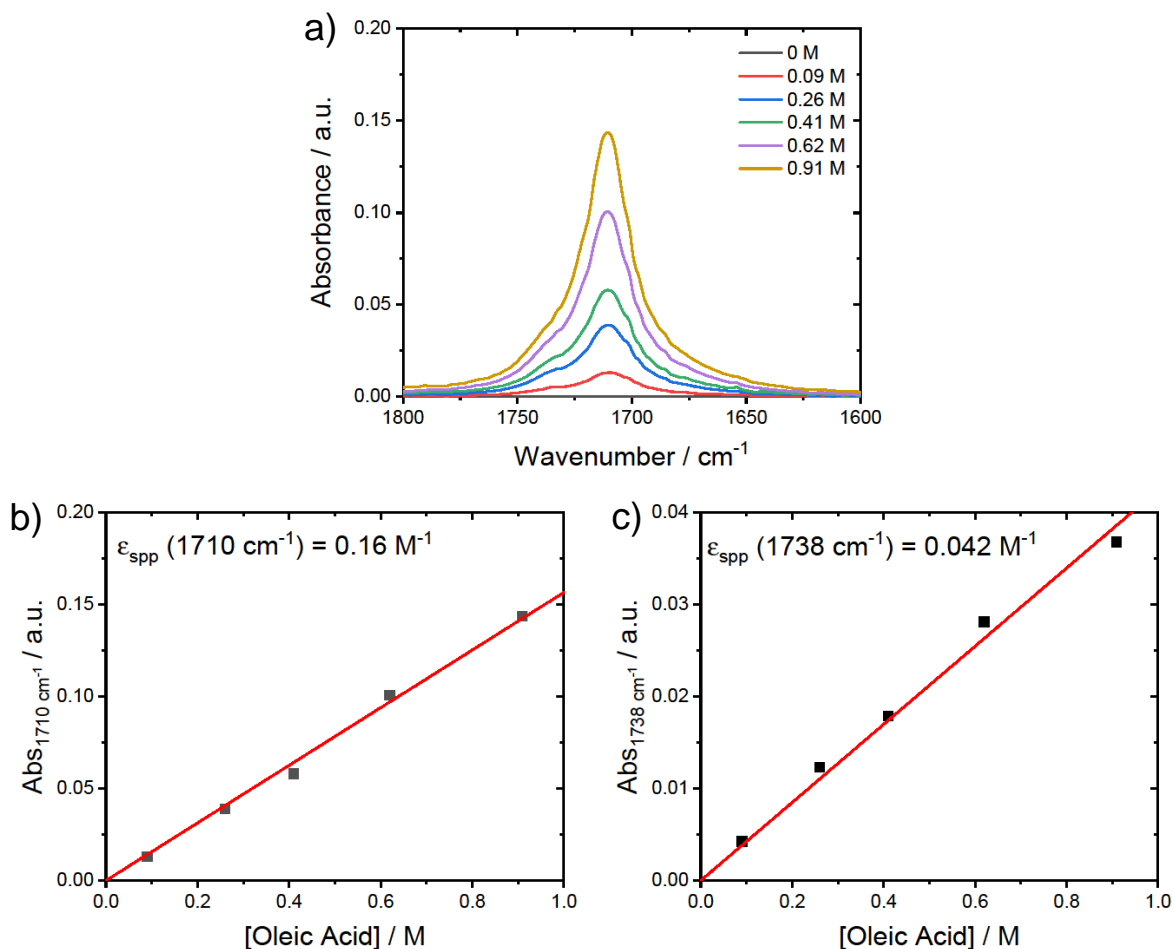


Figure S19. a) FTIR absorbance spectra of oleic acid dissolved in oleyl alcohol at controlled concentrations. Spectra are background corrected for oleyl alcohol. (b-c) Beer-Lambert plots for absorbance at 1710 and 1738 cm^{-1} with slopes of 0.16 and 0.04 M^{-1} , respectively. Despite not knowing the path length associated with the ATR-FTIR measurement, the linearity in these plots indicates a constant path length across different samples. Therefore, the slopes were used directly as apparent extinction coefficients for oleic acid in oleyl alcohol such that $\epsilon_{\text{app}}(1710 \text{ cm}^{-1}) = 0.16 \text{ M}^{-1}$ and $\epsilon_{\text{app}}(1738 \text{ cm}^{-1}) = 0.04 \text{ M}^{-1}$.

Supporting Information

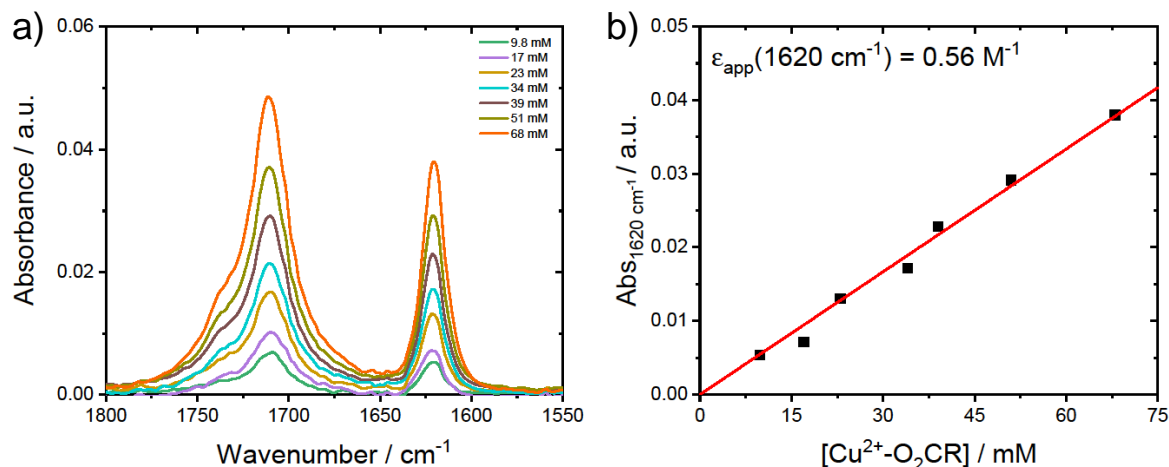


Figure S20. a) FTIR absorbance spectra of Cu²⁺-O₂CR dissolved in oleyl alcohol at controlled concentrations. Spectra are background corrected for oleyl alcohol. b) Beer-Lambert plot for absorbance at 1620 cm⁻¹ with a slope of 5.6 x 10⁻⁴ mM⁻¹. Despite not knowing the path length associated with the ATR-FTIR measurement, the linearity in these plots indicates a constant path length across different samples. Therefore, the slope was used directly as an apparent extinction coefficients for Cu²⁺-O₂CR in oleyl alcohol such that ε_{app}(1620 cm⁻¹) = 0.56 M⁻¹.

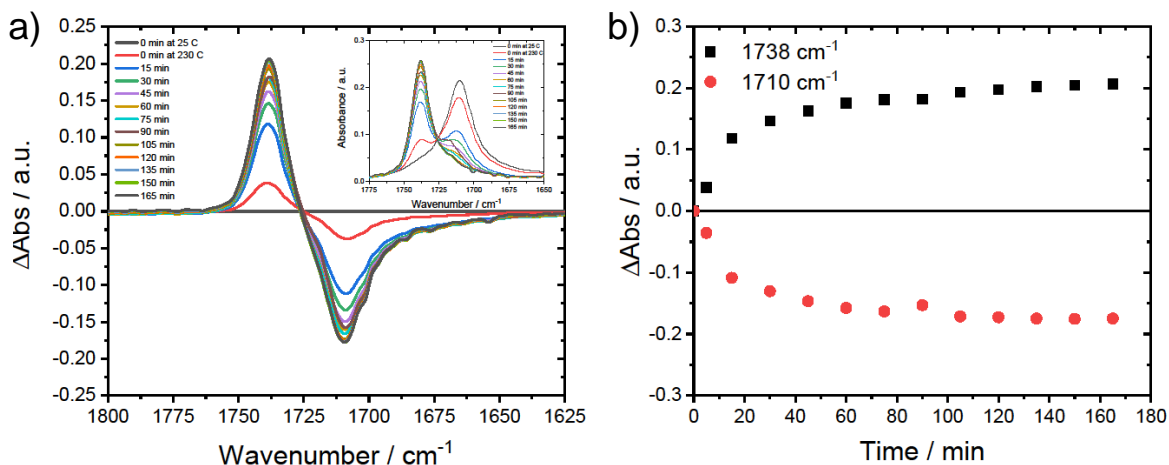


Figure S21. a) FTIR ΔAbs spectra of oleic acid dissolved in oleyl alcohol and heated to 230 °C. Time dependent spectra were generated by removing small aliquots from solution over the course of the reaction. ΔAbs data were generated by subtracting all spectra from the initial 0 min at 25 °C condition. Inset shows raw absorbance data. b) ΔAbs at 1710 and 1738 cm⁻¹ plotted versus time of reaction. The final time point at 165 min, representing complete conversion from acid to ester, was used to calculate apparent extinction coefficients for oleyl oleate ester based on the equation ΔAbs($\tilde{\nu}$) = Δε($\tilde{\nu}$)[Ester] where [Ester] = 1.27 M and Δε($\tilde{\nu}$) = ε_{ester}($\tilde{\nu}$) - ε_{acid}($\tilde{\nu}$). Resulting values were ε_{app}(1710 cm⁻¹) = 0.018 M⁻¹ and ε_{app}(1738 cm⁻¹) = 0.20 M⁻¹.

Supporting Information

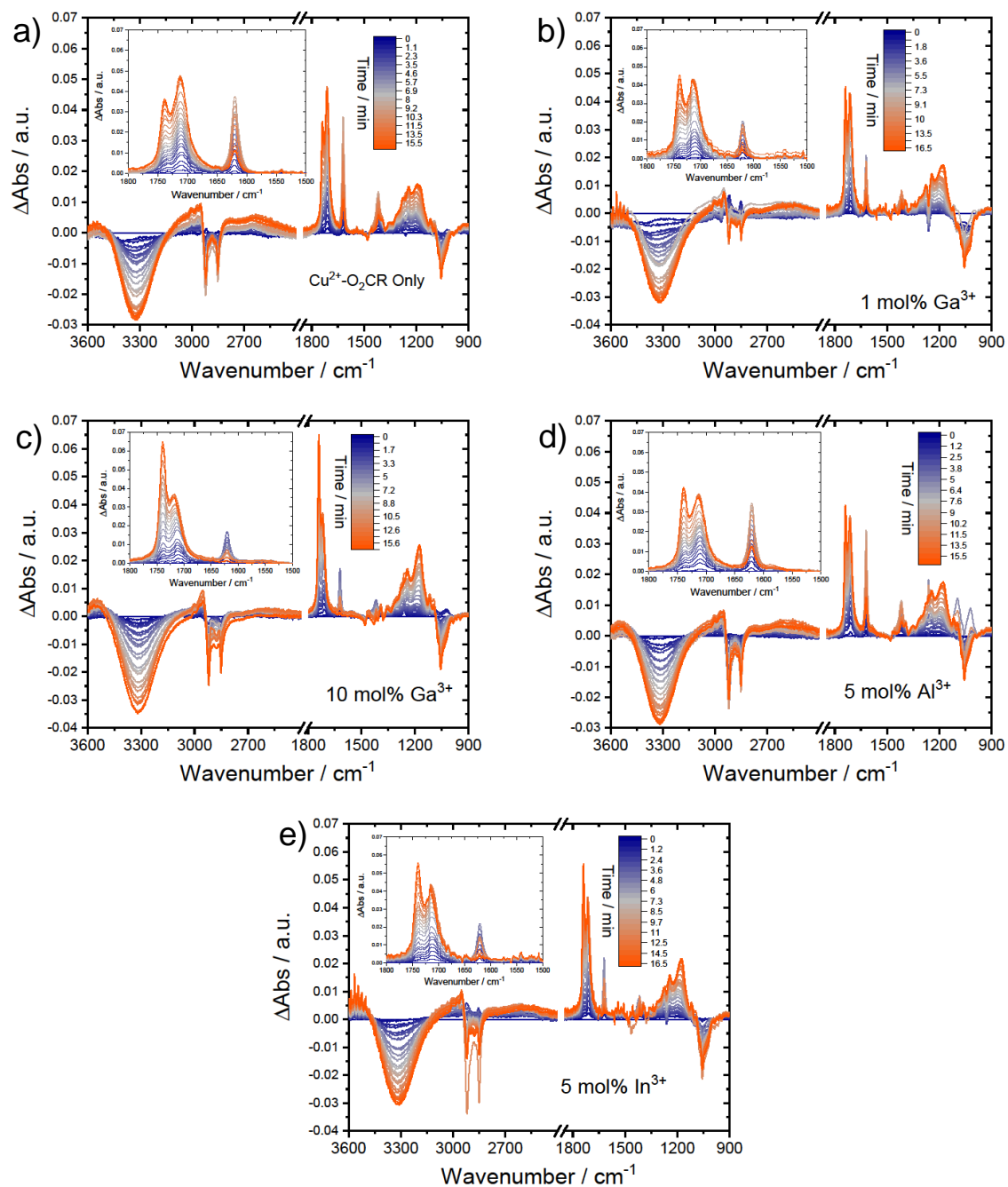


Figure S22. Time-dependent FTIR Δ Abs spectra for a) Cu^{2+} - O_2CR only injection, b) 1 mol% Ga^{3+} , 10 mol% Ga^{3+} , 5 mol% Al^{3+} , and 5 mol% In^{3+} catalyzed reactions. Δ Abs spectra generated by subtracting the initial spectrum at $t = 0$ min.

Supporting Information

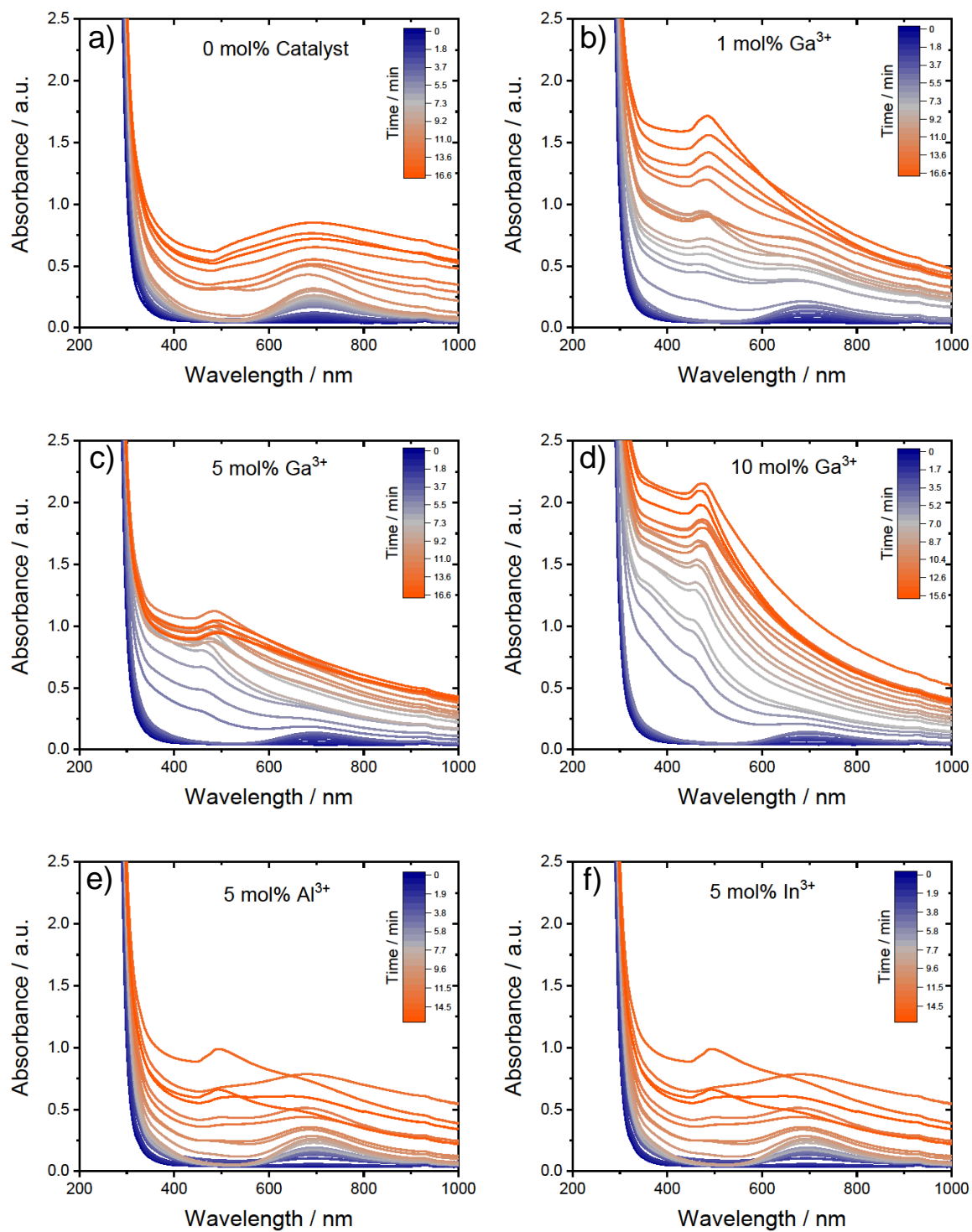


Figure S23. Time-dependent UV-visible absorbance spectra for a-d) 0-10 mol% Ga³⁺, e) 5 mol% Al³⁺ and f) 5 mol% In³⁺ catalyzed reactions.

Supporting Information

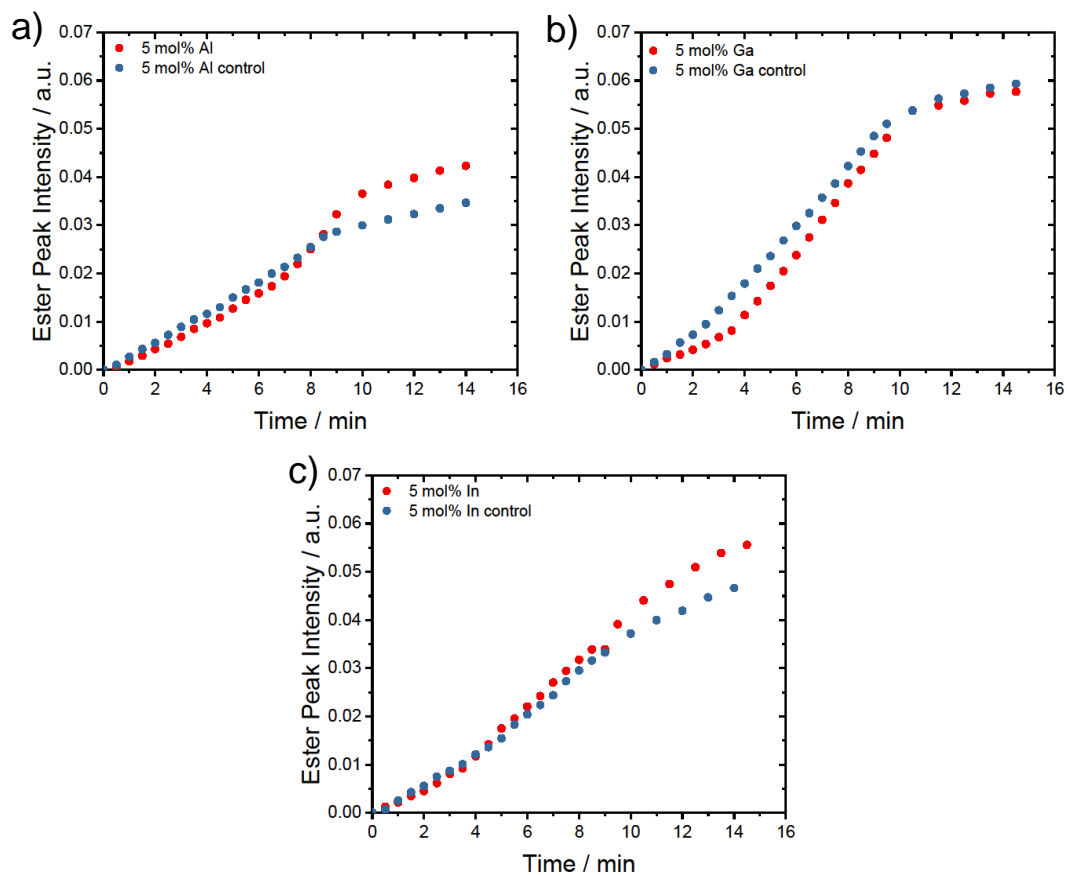


Figure S24. Comparison of FTIR ester peak absorbance at 1738 cm^{-1} measured over time for 5 mol% a) Al^{3+} , b) Ga^{3+} , and c) In^{3+} with and without (*i.e.* control) the presence of Cu^{2+} - O_2CR precursor.

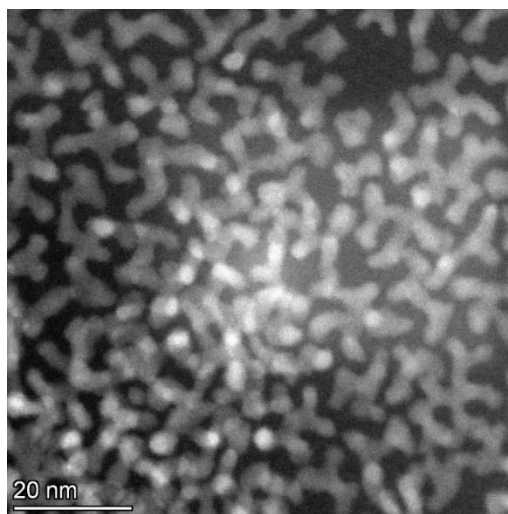


Figure S25. TEM HAADF image of In_2O_3 nanocrystals produced with 100 mol% injection of In^{3+} - O_2CR into oleyl alcohol at $200\text{ }^\circ\text{C}$.